Advances in Image And Video Processing

TABLE OF CONTENTS

DISCLAIMER

Statistical Analysis of the Characteristic Features of Standard Image for Racial and Ethnic Identity of a Person

Shafagat Mahmudova
Institute of Information Technology of ANAS, Baku, Az1141, Azerbaijan
shafagat_57@mail.ru

ABSTRACT

The paper provides statistical analysis of the characteristic features used to determine racial and ethnic identity of a person basing on the images. Standard characteristic features of the persons of each ethnic group have been set accordingly. Characteristic features of random image have been compared with the characteristic features of standard image to determine belonging of a person to this or that racial and ethnic group. Comparing the characteristic features of the random image with the characteristic features of the standard image of each ethnic group, it is important to define the reliability of the interdependence between them. Note that, characteristic features of standard image were determined basing on the characteristic features of a real human face belonging to each ethnic group. The dependence was defined among the characteristic features of racial and ethnic standards set up according to the images with the characteristic features of a human face. A Fischer criterion was used to determine the dependence.

Keywords: Fisher criterion, race, ethnicity, person, correlation

1   Introduction

Recently, modern information and communication technologies have developed rapidly. Emerging information society includes a number of important issues that have not been fully resolved and studied. One of these pressing issues is the racial and ethnic identification of a person basing on the images. Currently, specialists in various fields of science are dealing with this issue. The problems existing in this area have been partially solved by very few specialists using different methods.

Upon recognizing a person, a facial image (photo portrait) is of particular theoretical and practical value [1]. There is currently a significant number of articles devoted to recognize people based on portrait photographs]. However, there are much less works on the recognition of people based on their affiliation to an ethnic group is much less [2].

A new method is proposed to create a real three-dimensional portrait photograph based on the two-dimensional portrait for synthesis of two dimensional portrait photographs arbitrarily made in some works using special models prepared in accordance with gender and ethnicity [3].

Ethnicity is considered as a very important demographic characteristic for the humanity. Automatic ethnic classification based on human face is important in different fields. Some articles have research both two- and three-dimensional characteristics of the human face, MM-LBP multi-modal method (multi- scale multi-ratio) has been proposed for ethnic classification. LBP (Local Binary

Pattern) histograms were compiled from multi-scale multi-ratio quadrangular parts based on texture and range images [4].

Visual information such as gender, age, ethnicity and facial expression play an important role in face-to-face communication. Some articles have proposed a new approach for ethnic classification of the human face based on the portrait photograph. Gabor Wavelets Transformation identifying the main facial expressions and eye reticular membrane samples were combined in this approach. Support vector apparatus was used for ethnic classification. Using the system based on this approach, 94% ethnic evaluation was achieved in different lighting conditions [5].

Unlike existing models depending only on two-dimensional portrait photographs in some articles, a new method was proposed for solution of issues related to combination of local texture and form characteristics obtained using three-dimensional models of the face. Proposed method used Oriented Gradient Maps in order to demonstrate local geometric variations, as well as all texture variations of the face [6].

Specialists in Ethnography conduct research to solve existing problems in the field of humanities; and the experts in technical sciences study "Pattern recognition".

2   Problem statement

In the previous study, the author of the paper have developed an algorithm for the standard characteristic features to determine racial and ethnic identification basing on the images of people who have the same historical and ethnic features. Taking into account three generations of tribal and ethnic groups of the people with the same race and ethnicity, a database was formed based on their images. The standard image, i.e. the basic matrix of its characteristic features was formed by calculating selected geometric points of the face and characteristic features of the images in the database. Then, the characteristic features of the random image were compared with the characteristic features of the standard image of each racial and ethnic group, and belonging to any racial of ethnic group of the random image was defined [7-11].

It was decided to use 30 identification points during the preliminary tests.

Note that the characteristic features of the standard image were drawn up, based on characteristic features of the images of people of mongoloid, negroid and European race. And the standard characteristic features were compiled according to defined real features of the people belonging to racial and ethnic groups.

The task of determination of affiliation of the reference image to one of the l ethnical groups comes down to finding Euclidean distance among the matrix of $P^l(p_{ik}^l, i = 1,9, k(i,j) = 1,190)$ of l ethnical groups and the matrix of $P^*(p_{ik}^*, i = 1,9, k(i,j) = 1,190)$ of characteristic parameters of the reference image as following:

$$D_l = \sqrt{\sum_{i=1}^{9}\sum_{k=1}^{190}(p_{ik}^l - p_{ik}^*)^2} \ , l = 1,2,\dots$$

(1)

Further, the value of $D_{l*} = min(D_l, l = 1,2,..)$ determines the number of the ethnical groups with which the reference image is affiliated [12].

3   Solution algorithm

Dependence was compared with the characteristic racial and ethnic standards drawn up on the basis of the real characteristic features of the human face. Fischer criterion was used for this purpose. Fisher criterion (F) shows a reliable correlation. It is quite valid between more than two depended numeral variables. The correlation describes statistical relationship between two or more random variables. The change in one or more variables leads to a systematic change in the others. The correlation between the two variables is mathematically expressed in coefficients. The coefficients are negative or positive depending on the nature of the interaction. If the correlation is negative the increase in the value of one variable affects the decrease in the values of others, and vice versa. The values of the correlation coefficient vary between -1 and +1. If the value of the coefficient is close to 1 the relation is likely to be strong between the two variables. If the coefficient is close to 0 it is the weakest relation.

The correlation relation is calculated by the following formula:

$$\eta = \sqrt{\frac{\sigma^2}{\sigma_*^2}} \qquad (2)$$

For instance, racial and ethnic groups are $l\,(l = 1,2,\ldots)$. The database developed for each group includes male or female photos at the n_l number. Then, the matrix of characteristic features of the standard image $P^l(p_{ik}^l, i = 1,9, k(i,j) = 1,190)$ are defined for the l_i - th group as follows (tab.1):

$$p_{ik}^l = \sum_{j=1}^{n_l} w_{ik}^{jl} / n_l \qquad (3)$$

As a numerator of the radical a dispersion calculated for the real values of a human face is denoted by σ^2, and as a denominator empirical values, i.e. a dispersion of the characteristic features calculated according to the images of the human face are denoted by σ_*^2 and they are calculated by the following formula:

$$\sigma^2 = \frac{\sum_{i=1}^{9}\sum_{k=1}^{190}(p_{ik}^l - \overline{p}_{ik})^2}{n}, l = 1,2,\ldots \qquad (4)$$

$$\sigma_*^2 = \frac{\sum_{i=1}^{9}\sum_{k=1}^{190}(p_{ik}^{l*} - \overline{p}_{ik}^{*})^2}{n}, l = 1,2,\ldots \qquad (5)$$

i=1,9; k=1,190;

Here, ethnic group *l* indicates number of features *k*.

p_{ik}^l , p_{ik}^{l*} - is the value of the i-th theoretical (calculated) and empirical (actual) row;

$\overline{p}_{ik}$, $\overline{p}_{ik}^{*}$ - is the average value of theoretical (calculated) and empirical (actual) row.

n is the number of the members.

In conducted studies the form of relations is preferred, where the value of the correlation relationship is closer to 1.

Fisher criterion (F) indicates reliable correlation (it describes statistical relationship between two or more random variables). Fisher criterion is quite valid between more than two depended numeral variables.

The values of Fisher criterion are calculated by the following formula:

$$F = \frac{\dfrac{\sum\limits_{i=1}^{9}\sum\limits_{k=1}^{190}(p_{ik}^{l} - \overline{p}_{ik})^2}{n-1}}{\dfrac{\sum\limits_{i=1}^{9}\sum\limits_{k=1}^{190}(p_{ik}^{l*} - \overline{p}_{ik}^{*})^2}{n-m-2}} , \tag{6}$$

$$F = \frac{\sigma^2}{\sigma_*^2} , \tag{7}$$

m is the number features taken into account in the model (independent variables).

The mean-square relative error of actual variables found from the calculation is calculated by the formula:

$$m^{'} = 100.\sqrt{\dfrac{\sum\limits_{i=1}^{9}\sum\limits_{k=1}^{190}(\dfrac{p_{ik}^{l} - \overline{p}_{ik})^2}{p_{ik}^{l}}}{n}} , \tag{8}$$

The mean-error approximation ($\overline{\varepsilon}$) calculated by the formula:

$$\overline{\varepsilon} = \frac{1}{n}\sum\limits_{i=1}^{9}\sum\limits_{k=1}^{190}(\frac{p_{ik}^{l} - \overline{p}_{ik})^2}{p_{ik}^{l}} . 100 \tag{9}$$

Both indicators characterize the degree of accuracy of reflecting the real number by these models.

The size of correlation relations, Fischer criterion, the mean-square error and mean error approximation are reduced.

The approximation or approaching is a research method, in which one object is replaced by another, in other words, is closer to the primary variable, but is relatively simple.

4   Identification system

"Racial-ethnic" biometric identification system (REBIS) was established for the recognition of a person's racial or ethnic origin.

Numerous experiments were carried out through IEBIS. The database includes images of different sizes of the people belonging to different races at *n* number. An algorithm was developed in order to add automatically the values of characteristic features to the database, which are used for the racial and ethnic identification of a person on the basis of images, and in order to search and identify the human face on the basis of his image in the database. The front page of REBIS is shown in Figure 1.

Experimental tests were carried out by using the images of FERET database.

Value of dispersion and the standard error for race groups is shown in Table 1 and diagram in Figure 2.

The distances calculated automatically in accordance with the characteristic points, which are determined on the basis of the image of each human face, are included and saved into the database. This data is included into the database once and can be modified.

For the successful racial and ethnic recognition of a person on the basis of face images a number of issues need to be solved:

1. Choosing the anthropometric points of human face on the basis of template;
2. Calculating the geometric features according to the characteristic points of the random face images given for the recognition, and adding them into the database automatically;
3. The recognition process should not depend on the image scale;
4. Realizing the recognition of human face and informing the user about it.

The main difference of REBIS from the others is its high speed processing by means of developed algorithm, efficient use of images stored in the database and its prompt recognition. The main advantage of the proposed algorithm is the resistance of the results to the change in the person's appearance depending on his aging. The experiences were carried out on more than 150 people of European, negroid and mongoloid race, and 96 - 98% recognition accuracy has been achieved by means of developed algorithm. Identification process carried out through REBIS is more rapid, saving time.

Entering the REBIS an image of a person of any racial group is given, in the output of the proposed system the racial and ethnic identification of the given person is determined.

Figure 1: The front page of REBIS

Table 1. Value of dispersion and the standard error

	European	Mongoloid	Neqroid	Any person
Dispersion	0,35	0,44	0,47	0,37
The standard error	0,36	0,45	0,49	0,38
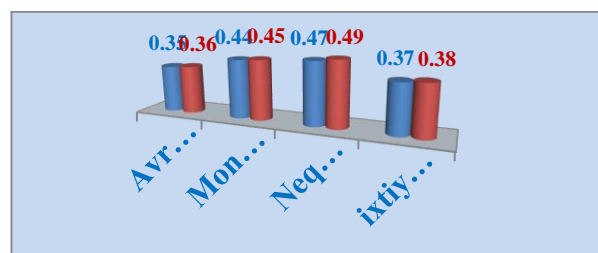
Figure 2: Diagram of Value of dispersion and the standard error for race

5   Results

The paper informs about the application of Fisher criterion to define the dependence of the features, which are used for racial and ethnic identification of a person on the basis of images. Note that, characteristic features of standard image were determined basing on the characteristic features of a real human face belonging to each ethnic group. The dependence was defined among the characteristic features of racial and ethnic standards set up according to the images with the characteristic features of a human face. The recognition tests gave promising results.

The dependence forms meeting the following requirements are preferred:

- The highest coefficient of multiple correlations;
- Higher Fischer criterion;
- Mean-square error is smaller.

Theoretical studies and practical results of recognition by national - racial affiliation based on the portrait photographs can be used in the interests of the many professions that require adequate recognition of people (customs, border control, security, etc.). Upon determining the identity based on identification systems, the basis of which contain several millions of portraits – will significantly narrow the search area while reducing the time of recognition.

REFERENCES

[1]   L.R., Adilova, on face recognition//Intellectual systems, vol. 14. Moscow, 2010, pp. 73-84.

[2]   Alberto Del Bimbo, Pietro Pala, Stefano Berretti, Distinguishing Facial Features for Ethnicity-Based 3D Face Recognition // ACM Transactions on Intelligent Systems and Technology (TIST), 2012, pp. 1-20.

[3]   Jingu Heo, M., Savvides, Gender and Ethnicity Specific Generic Elastic Models from a Single 2D Image for Novel 2D Pose Face Synthesis and Recognition // IEEE Transactions on Pattern Analysis and Machine Intelligence (TPAMI), vol. 34, 2012, pp. 2341-2350.

[4]   Guangpeng Zhang, Yunhong Wang, Multimodal 2D and 3D Facial Ethnicity Classification // Fifth International Conference on Image and Graphics. China September 20 – 23, 2009.

[5]   Satoshi Hosoi, Erina Takikawa, Masato Kawade, Ethnicity Estimation with Facial Images / Sixth IEEE International Conference on Automatic Face and Gesture Recognition (FG'04), Seoul, Korea, May 17-19, 2004.

[6]   Huaxiong Ding, Liming Chen, Facial ethnicity classification based on boosted local texture and shape descriptions / 2013 10th IEEE International Conference and Workshops on Automatic Face and Gesture Recognition (FG). Shanghai, China, April 22- 26, 2013.

[7]   T. H., Kazımov, Sh.J., Mahmudova, About creation of system of computer recognition of people by photographs / Proceedings of the Fifth International Conference on Neural Networks and Artificial Intelligence, May 27-30, 2008, Minsk, pp. 164-167.

[8]   T. G., Kyazimov, Sh. Dzh., Mahmudova, The Effectiveness Increase of a System of Automatic Biometrical Identification Based on Photo Portraits // Automatic Control and Computer Sciences, 2011,Vol. 45, No. 2, USA, pp. 106–112.

[9]   Sh.J., Mahmudova, Definition of weight coefficient of geometric characteristics used for identification of human face on the basis of photo-portrait / Proceedings of the 6th 2011 International Conference on Computer Sciences and Convergence Information Technology, Nov. 29 – Dec. 1, Jeju Island, Republic of Korea, IEEE Press, 2011, pp. 797-802.

[10]   T. H., Kazımov, Sh.J., Mahmudova, About a Method of Calculation of Importance Degree of Geometrical Characteristics to Identify a Human Face on the Basis of Photo Portraits // Computer Science and Engineering, 2012,Vol. 2, No. 5, USA, pp. 59-62.

[11]   T. H., Kazımov, Sh.J., Mahmudova, About A Method of Calculation of Importance Degree of Geometrical Characteristics to Identify a Human Face On The Basis Of Photo Portraits / Proceedings of the 7 th IAPR International Conference on Pattern Recognition in Bioinformatics, 2012, November 8-10, Tokyo, pp. 154-160.

[12]   T. H., Kazımov, Sh.J., Mahmudova, Increase of indicator values of identification systems quality on the recognition of human face on the basis of photoportraits // Intelligent Control and Automation, 2013,Vol. 4, No. 2, USA, pp. 191-198.

An Efficient Implementation of Acute Lymphoblastic Leukemia Images Segmentation on the FPGA

[1]Kamal A. ElDahshan, [2]Mohammed I. Youssef, [3]Emad H. Masameer and [4]Mohammed A. Mustafa

[1,3]*Mathematics Department, AL-AZHAR University, Cairo, Egypt;*
[2]*Electronic Engineering Department, AL-AZHAR University, Cairo, Egypt;*
[4]*MIS Department, Modern Academy for Computer Science and Information Technology, Cairo, Egypt*
dahshan@gmail.com; mohiyosof@yahoo.com; emadmasameer@yahoo.com;
mohammedsecret@gmail.com

ABSTRACT

In the medical field, image segmentation process is considered the most essential step in image analysis. In this work, the color segmentation for acute lymphoblastic leukemia images (ALL) is applied to segment each leukemia image into two clearly defined regions: blasts and background. The ALL segmentation process is based on hue channel (H) of HSV color space as a method in segmentation of WBC from its complicated background. This work presents an efficient framework for segmentation of ALL images on a reconfigurable logic platform using Simulink, MATLAB and Xilinx System Generator (XSG). This segmentation framework is implemented on a FPGA using basic Xilinx Blockset to minimize hardware resources and lower execution time to be suitable enough for medical applications. It is designed using XSG as DSP design tool that enables the use of Simulink models, implemented in VHDL and synthesized for three different Xilinx FPGA boards.

Keywords: Color segmentation, FPGA, ALL, XSG.

1   Introduction

The term Leukemia refers to a group of cancers resulting from abnormal increase of the white blood cells (WBCs) that divided and grew in uncontrolled way. These WBCs start from the bone marrow and shift quickly into the blood to reach to other parts of the body such as spleen, lymph nodes and liver. Thus, early diagnosis and treatment applied to these WBCs are vital.

Leukemia can be categorized into: acute and chronic. Acute leukemia spreads very quickly and has to be treated immediately rather than chronic leukemia where immediate treatment is not a must. Also, acute leukemia can be either lymphoblastic (ALL) or myelogenous (AML), based on affected cell type. Chronic leukemia can be either lymphoblastic (CLL) or myelogenous (CML) [1]. Acute lymphoblastic leukemia (ALL) is considered to be the main focus of this work because the survival rate is expected to be higher when other types.

According to image processing field, segmentation process is considered the most demanding tasks. It is used to partitioning a digital image into a number of different meaningful regions. For biomedical imaging applications, image segmentation is a founding step in image analysis [2] as it will directly affect the post-processing. It is a crucial component in diagnosis [3] [4] and treatment [5].

The main aim of acute leukemia blood cell segmentation is to extract component such as WBCs from its complicated background. There are many techniques that have been developed for image segmentation [6] [7] [8]. Due to the complex nature of blood cells and overlapping between these cells, segmenting them remains a challenging task [9]. Many algorithms for segmentation have been developed for color images that produce more information of the scene than grayscale images do [10]. For leukemia segmentation process, transformations of original RGB images to different color spaces such as (HSI, HSV, YUV, XYZ, Lab…etc.) are proposed in many works. According to [11], Lab color space is used for segmentation process. Also, algorithm based on HSI color space is proposed in [12]. Based on HSV color space, segmentation technique [13] for ALL images is proposed.

Image processing algorithms implemented in FPGA have emerged as the most viable solution for improving the performance of image processing systems. It offers a compromise between the flexibility of general purpose processors and ASICs. FPGAs are recently used in many image processing applications such as image compression [14] [15] [16] [17], image filtering [18] [19] and wireless communication [20] [21] [22]. Xilinx System Generator is a DSP design tool [23] [24] that deal with many images processing application. XSG is a part of the ISE design suite that provides Xilinx DSP Blockset for application specific design. The main advantage of using Xilinx system generator for FPGA implementation is that Xilinx blockset provides close integration with MATLAB Simulink that helps in co-simulating the FPGA module with pixel vector provided by MATLAB Simulink Blocks [25].

This work focuses on implementing multilevel thersholding segmentation technique efficiently based on color histogram of H channel of HSV color space on FPGA using basic Xilinx blockset. Firstly, all algorithms are implemented in MATLAB to realize the segmentation results. The pipelined framework of multilevel thersholding image segmentation is implemented on three FPGA devices Spartan3E xc3s500e-4fg320, Spartan 3A DSP 3400A-4fg676 and Spartan 3AN xc3s700an-5fgg484.

2   Proposed Framework

A typical acute lymphoblastic leukemia sample consists of three main regions: abnormal white blood cells (blast), red blood cell (RBC) and background areas. Nucleus and cytoplasm regions formed a blast and contain important information to be observed by hematologists. However, the RBC and background regions contain no information and can be eliminated from the image. In this work, the proposed framework is divided into two main parts. The first part is to apply the color image segmentation technique on ALL images using HSV color space. For the second part, this segmentation technique is implemented on FPGA using basic Xilinx blockset. The proposed framework involves the following steps:

2.1   Image Database

Microscope Images of ALL are taken from ALL-IDB database [26]. An optical laboratory microscope together with a Canon Power Shot G5 camera was used to capture the images of the database. In addition, all images are in JPG format with 24 bit color depth, resolution 2592 × 1944. Moreover, the images are taken with different magnifications of the microscope ranging from 300 to 500. ALL-IDB2 version of the database is used as well. Figure 1 shows the sample of ALL images.
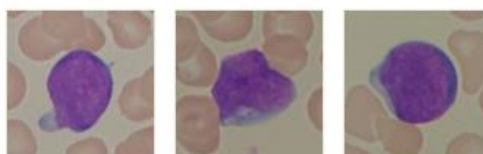
Figure 1: Sample of ALL images

2.2   Acute Lymphoblastic Leukemia Segmentation

According to the inherent interdependence between luminance and chrominance in the RGB color space, a HSV color space is used. HSV provides useful chromatic information of the image that located in a single channel without any luminance effect. Also, HSV color space is familiar to human perception and more suitable for image processing than RGB color space [27]. HSV color space contains three channels. The hue (H) channel refers to the color type such as (Red, Green, Yellow…etc.). The range of hue values changes from 0º to 360º passing throw rainbow colors. Saturation (S) value affects the purity of the colors while Value (V) means the amount of light in the color. Both S and V range from 0 to 1. H channel that only needed for ALL segmentation process is obtained by transforming the source image from RGB color space to HSV color space based on the following equations:

$$H = \begin{cases} 0 & \text{if M} = \text{ m} \\ \left(60^O X \dfrac{g-b}{M-m} + 0^O\right) \bmod 360^O & \text{if M} = \text{r} \\ 60^O X \dfrac{b-r}{M-m} + 120^O & \text{if M} = \text{g} \\ 60^O X \dfrac{r-g}{M-m} + 240^O & \text{if M} = \text{b} \end{cases}$$

Where:
M means the maximum values in R, G, and B elements.
m means the minimum values in R, G, and B elements.

To segment ALL images into blasts and background using H channel of HSV color space. There are 6 steps involved in applying image segmentation process as shown in figure 2.
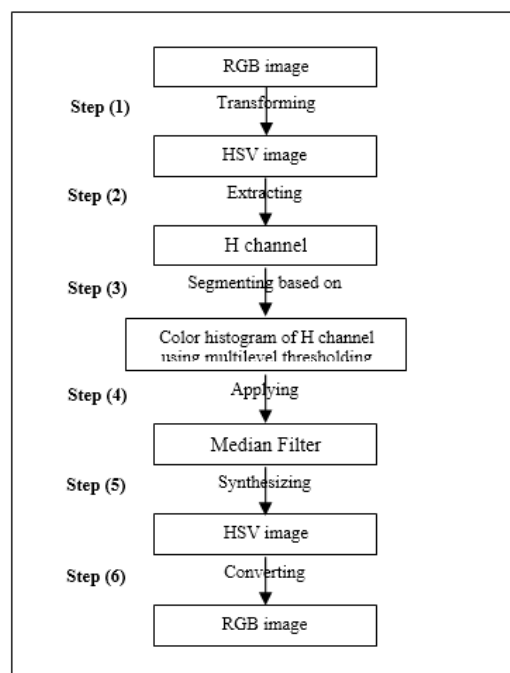
Figure 2: Block diagram of ALL segmentation using HSV

2.3 FPGA Implementation

Although computers keep getting faster and faster, there are always new image processing applications that need more processing than is available. Field Programmable Gate Arrays are very capable devices in the area of digital signal processing. They are semiconductor devices that contain a number of logic blocks, which can be programmed to perform complex image processing algorithms. The main purpose of this work is to implement color image segmentation technique on a FPGA more efficient than [28] by using only basic Xilinx blockset. Segmentation based on FPGA is designed using XSG that enables the use of Simulink models and implemented using VHDL.

Due to the implementation process based on FPGA, the pre-processing and post-processing steps for ALL segmentation are proposed using Simulink blocks. Figure 3 presents color space conversion block from RGB to HSV image and applying median filter to H channel for further processing.
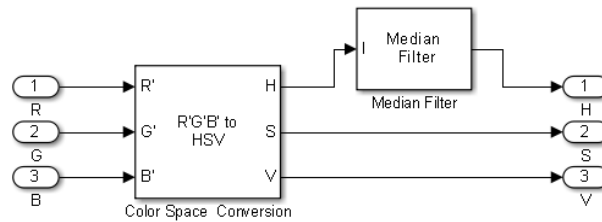
Figure 3: Pre-processing for ALL segmentation

To accomplishing Image processing task using Xilinx System Generator, two Software tools are needed to be installed. This work uses MATLAB version R2012b and Xilinx ISE 14.5. The model is built for image segmentation using library provided by Xilinx Blockset. According to the design of segmentation to meet FPGA requirements, pre-processing the HSV image prior to the main FPGA framework is needed due to the nature of FPGA that deals with an image as a vector. Also, image post-processing is required. There are three stages involved in ALL FPGA segmentation process using Simulink and Xilinx blocks:

- FPGA pre-processing
- Xilinx models for FPGA segmentation
- FPGA post-processing

Figure 4 represents the main block diagram of FPGA segmentation framework.
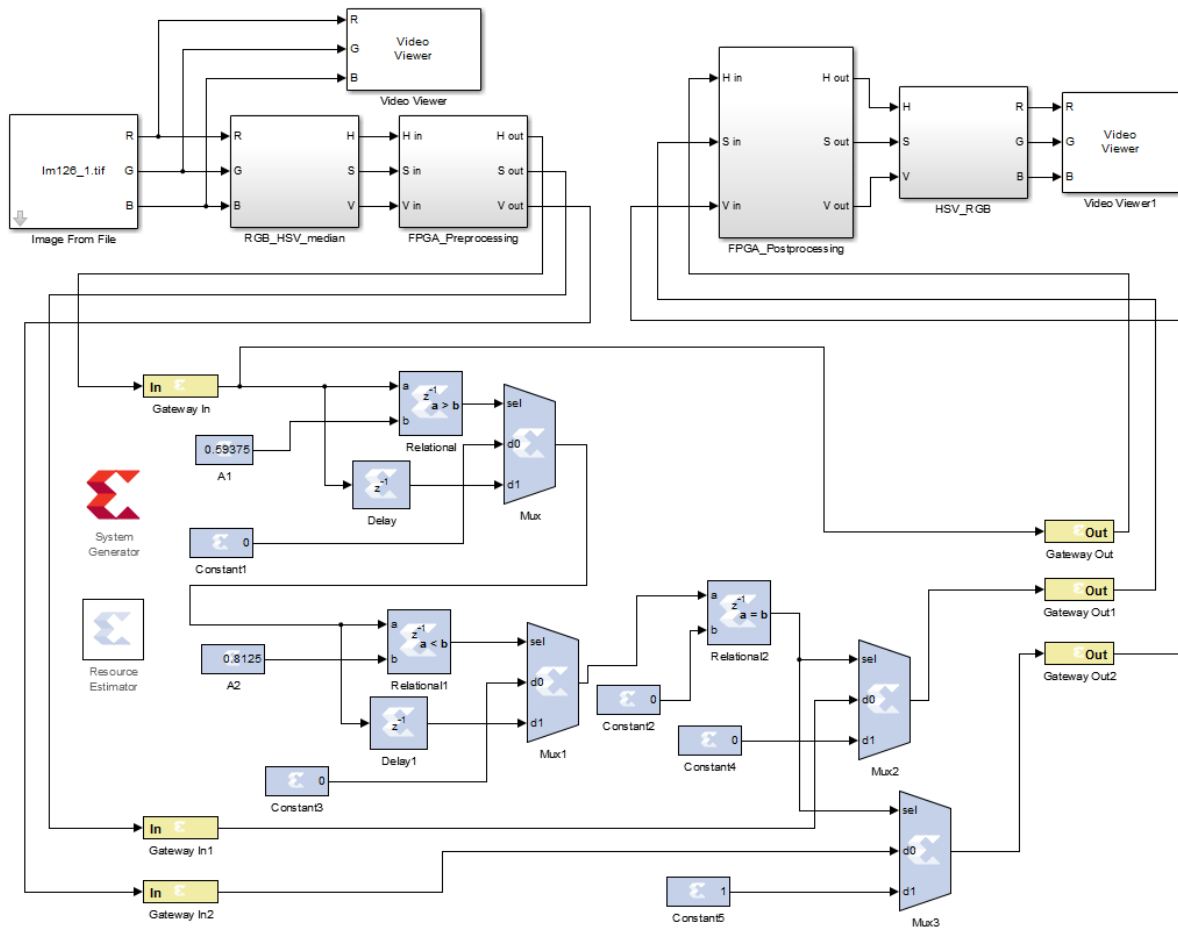
Figure 4: Block diagram of proposed framework

The image pixels are provided to Xilinx models in the form of multidimensional H|S|V separate color signals in the form of vector in Xilinx fixed point format. The reflected results can be seen on a video viewer. Once the expected results are obtained, XSG is configured to be suitable for SPARTAN-3E Starter kit xc3S500e-fg320, SPARTAN 3A DSP 3400A-4fg676 and SPARTAN 3AN xc3s700an-5fgg484 FPGAs.

2.3.1   FPGA Pre-Processing

Pre-processing blocks provide an input image suitable for FPGA as vector array. Reshape blocks convert the HSV image channels into single array of pixels. The process of setting sampling mode is obtained using frame conversion. Unbuffer blocks convert this frame to scalar samples output at a higher sampling rate. The model based design used for image pre-processing for FPGA is shown in Figure 5.
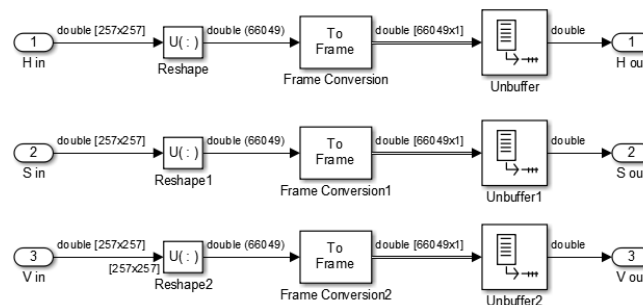
Figure 5: FPGA Pre-processing

2.3.2 Xilinx Models for FPGA Segmentation

FPGA segmentation process is modeled using Xilinx blocks. Once the FPGA boundaries have been established using the Gateway In and Gateway Out blocks, the DSP design can be constructed using Xilinx DSP blocks. Within the Gateway In and Gateway Out blocks, Simulink blocks are not supported for use.

Xilinx fixed point type conversion is made by Gateway In blocks. Image Segmentation process is achieved based on two angle values that obtained from color histogram of H channel. These two values are represented using two constant blocks. Multilevel thersholding operated using Relational and Mux blocks. This is followed by certain blocks to merge all the processed data. Figure 6 shows the ALL segmentation using basic Xilinx blocks while figure 7 presents ghost image using basic Xilinx blocks.
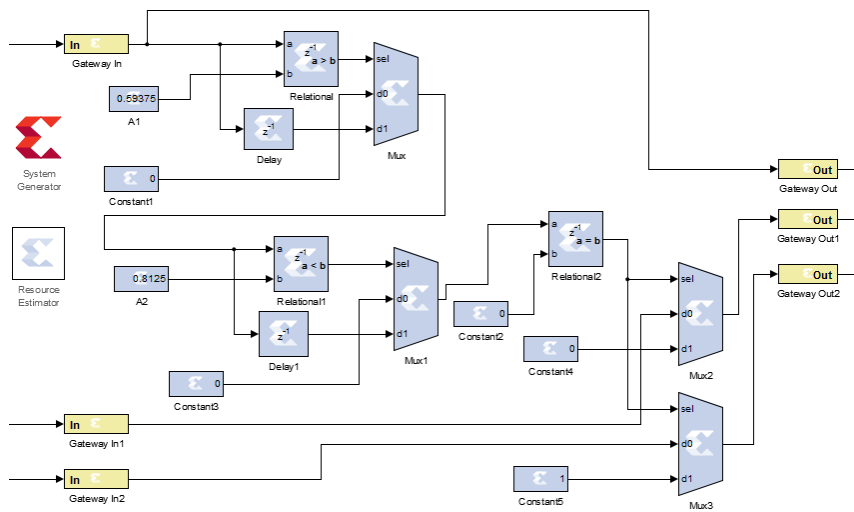
Figure 6: Segmentation of ALL images using standard Xilinx blocks
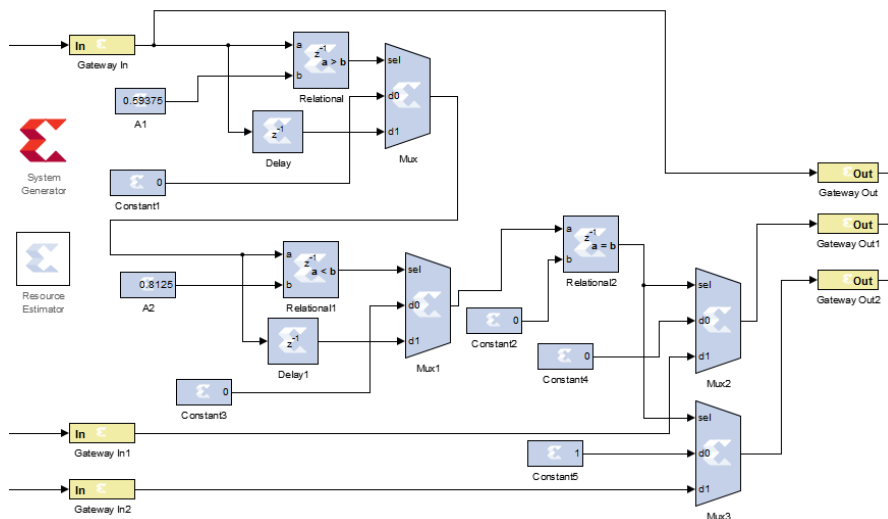
Figure 7: Ghost image for ALL using standard Xilinx blocks

2.3.3 FPGA Post-Processing

Post-processing blocks converts an image from vector to 2D matrix as shown in figure 8. Buffer blocks are used to convert scalar samples to frame output at lower sampling rate. The process of converting 1D image to 2D image is obtained using reshape blocks.
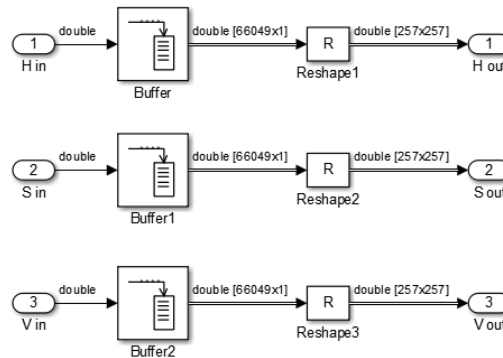
Figure 8: FPGA Post-processing

2.4 FPGA Co-Simulation

Once the results are obtained from FPGA design; the model is implemented for JTAG FPGA co-simulation. The system generator parameters are set and generated. On compilation, programming file in VHDL is created to be accessed by Xilinx ISE. The module is synthesized and implemented on FPGA. Figure 9 illustrates the FPGA co-simulation block.
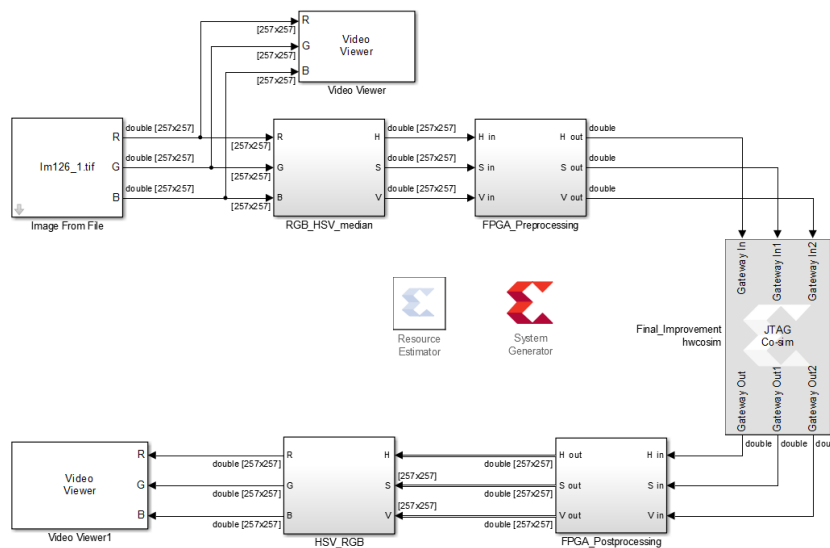
Figure 9: FPGA co-simulation

3 Results and Discussion

The segmentation framework based HSV color space described above is tested on two blood samples of ALL. The results obtained after applying proposed framework are shown in figure 10:

Original RGB images	**Segmented images**	**Ghost images**

Blood Sample 1

(a)   (b)   (c)

Blood Sample 2

(d)   (e)   (f)
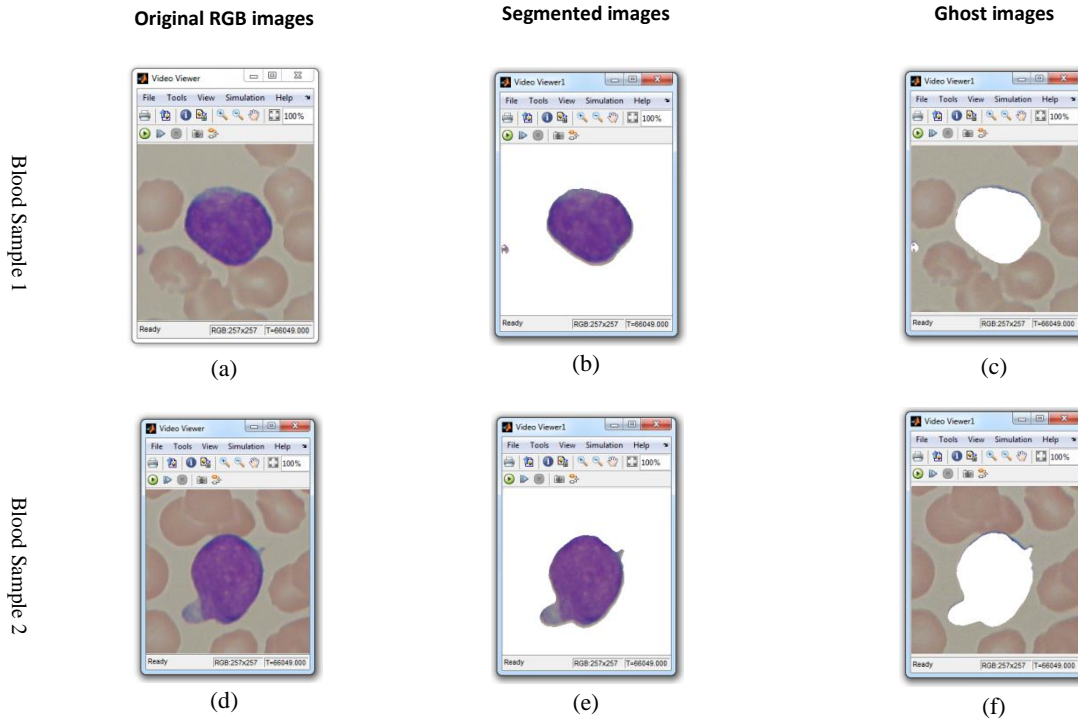
Figure 10: Segmentation of ALL Based HSV Color Space

Figure 10 (a) and figure 10 (d) represent the original RGB acute leukemia images. Meanwhile, figure 10 (b) and figure 10 (e) shows the output images after blasts segmentation process. Finally, Figure 10 (c) and figure 10 (f) show the ghost images for segmented images.

For FPGA implementation process, SPARTAN-3E Starter kit xc3S500e-fg320, SPARTAN 3A DSP 3400A-4fg676 and SPARTAN 3AN xc3s700an-5fgg484 resource usage is estimated for proposed framework as shown in table 1. The VHDL code for the proposed FPGA segmentation has 2381 lines of VHDL code. This is due to the huge amount of floating point-fixed point conversions.

Table 1: FPGA resources used in the implementation for ALL segmentation

	Spartan3E xc3s500e-4fg320		Spartan 3A DSP 3400A-4fg676		Spartan 3AN xc3s700an-5fgg484	
	Used	Available	Used	Available	Used	Available
Number of Slices Flip Flop	23	9312	23	47744	23	11776
Number of Occupied Slice	30	4656	27	23872	34	5888
Number of 4 input LUTs	40	9312	40	47744	40	11776
Number of Bonded IOBs	61	232	61	469	61	372
Maximum Frequency	291.72 MHz		310.17 MHz		366.845 MHz	

4   Conclusion

In this work, a performance comparison using image segmentation framework that applied on three FPGA devices for ALL blast detection is performed. The improved segmentation framework that implemented on FPGA is designed using only basic Xilinx Blockset. The design of FPGA segmentation framework implemented on SPARTAN 3AN xc3s700an-5fgg484 achieves 2.726 ns at 366.85 MHz as best minimum period. The design framework used in this work can be used for all Xilinx FPGA Kits. In the future work, the result of this work can be used as the basis for features extraction from the acute lymphoblastic leukemia blood samples.

REFERENCES

[1]   G. C. C. Lim," Overview of Cancer in Malaysia", Japanese Journal of Clinical Oncology, Department of Radiotherapy and Oncology, Hospital Kuala Lumpur, Kuala Lumpur, Malaysia,2002.

[2]   J.Rawat, A.Singh, H.S.Bhadauria, I.Kumar,"Comparative analysis of segmentation algorithms for leukocyte extraction in the acute Lymphoblastic Leukemia images", Parallel, Distributed and Grid Computing (PDGC), 2014 International Conference on, vol., no., pp.245,250, 11-13,2014.

[3]   P. Taylor,"Invited review: computer aids for decision-making in diagnostic radiology - a literature review", Brit. J. Radiol.., 68:945–957,1995.

[4]   C.T.N.Suzuki, J.F.Gomes, A.X.Falcao, S.H.Shimizu, J.P.Papa,"Automated diagnosis of human intestinal parasites using optical microscopy images", Biomedical Imaging (ISBI), 2013 IEEE 10th International Symposium on , vol., no., pp.460,463, 7-11, 2013.

[5]   V.S. Khoo, et al,"Magnetic resonance imaging (MRI): considerations and applications in radiotheraphy treatment planning", Radiother. Oncol., 42:1–15, 1997.

[6]   Q. Liao, Y. Deng,"An Accurate Segmentation Method for White Blood Cell Images", In IEEE International Symposium on Biomedical Imaging,pp.245-248, 2002.

[7]   V. Piuri, F. Scotti,"Morphology Classification of Blood Leucocytes by Microscope Images", In IEEE International Conference on Computational Intelligence International Conference on Image, Speech and Signal Analysis, 1992, pp. 530–533, 2004.

[8]   N. Venkateswaran, Y. V. Ramana Rao,"K-means Clustering Based Image Compression in Wavelet Domain", Journal of Information Technology: 148-153, 2007.

[9]   S. Mao-jun, et al.,"A New Method for Blood Cell Image Segmentation and Counting Based on PCNN and Autowave", in ISCCSP 2008 Malta, 2008.

[10]   Aimi Salihah , A.N, M.Y.Mashor , Nor Hazlyna Harun," Colour Image Enhancement Techniques for Acute Leukemia Blood Cell Morphological Features ", IEEE pp.3677-3682, 2010.

[11]   S. Mohapatra and D. Patra,"Automated Cell Nucleus Segmentation and Acute Leukemia Detection in Blood Microscopic Images", in International Conference On Systems In Medecine and Biology , India, 2010.

[12]   N. H. A. Halim, et al.,"Nucleus segmentation technique for acute leukemia", in Proceedings of the IEEE 7th International Colloquium on Signal Processing and Its Applications (CSPA '11), pp. 192–197, March 2011.

[13]   K.A. Eldahshan, et al.,"Segmentation Framework on Digital Microscope Images for Acute Lymphoblastic Leukemia Diagnosis based on HSV Color Space", International Journal of Computer Applications, 90(7): 2014.48-51, 2014.

[14]   J. Rosenthal,"JPEG Image Compression Using an FPGA", MS thesis, Dec 2006.

[15]   Y. Kim, K. Jun and K. Rhee.,"FPGA Implementation of Subband Image Encoder Using Discrete Wavelet Transform", IEEE TENCON, 1999.

[16]   S. K.Shah, R. K.Soni and B. Shah,"FPGA Implementation of Image Compression using bottom- up approach of Quad tree technique", IETE Journal of research , Vol 57, Issue 2, Mar-Apr 2011.

[17]   Yan Yaqiong; Zou Ruibin; Shi Caicheng,"JPEG2000 compression and decompression system based on Bayer image", Electronic Measurement & Instruments (ICEMI), 2013 IEEE 11th International Conference on , vol.2, no., pp.938,942, 16-19, 2013.

[18]   D. Rao, S. Patil, N. Babu and V. Muthukumar,"Implementation and Evaluation of Image Processing Algorithms on Reconfigurable Architecture using C-based Hardware Descriptive Languages", International Journal of Theoretical and Applied Computer Sciences,Volume 1 Number 1, pp. 9–34, 2006.

[19]   Nelson,"Implementation of Image Processing Algorithms on FPGA hardware", MS thesis, 2000.

[20]   H. Taha, A. Sazish, A. Ahmad, M. Sharif and A. Amira,"Efficient FPGA Implementation of a Wireless Communication System Using Bluetooth Connectivity", IEEE, 2010.

[21]   R. Mehra and S. Devi,"Efficient hardware co-simulation of down converters for wireless communication systems", International journal of VLSI design & Communication Systems (VLSICS), Vol.1, No.2, . June 2010.

[22]   Cheolgi Kim, Mu Sun, M.Rahmaniheris, Lui Sha,"How to reliably integrate medical devices over wireless", Sensor, Mesh and Ad Hoc Communications and Networks (SECON), 2012 9th Annual IEEE Communications Society Conference on , vol., no., pp.85,87, 18-21, 2012.

[23]   Z. Shanshan and W. Xiaohong,"Vehicle Image Edge Detection Algorithm Hardware Implementation on FPGA", International Conference on Computer Application and System Modeling ,ICCASM, 2010.

[24]   "Xilinx System Generator User's Guide", downloadable from;http:// www. Xilinx.com, 2010.

[25]   "Xilinx System Generator User's Guide", www.Xilinx.com , www.Xilinxforum.

[26]   R. Donida Labati, V. Piuri, F. Scotti,"ALL-IDB: the Acute Lymphoblastic Leukemia Image DataBase for image processing", 2011.

[27]   R. S. Ledley, M. Buas, & T. J. Colab,"Fundamentals of true-color image processing", Proc. 10th IEEE Conf. on Pattern Recognition, Los Alamos, CA, USA, 1990.

[28]   K.A. Eldahshan, et al.," Hardware Segmentation on Digital Microscope Images for Acute Lymphoblstic Leukemia Diagnosis Using Xilinx System Generator", International Journal of Advanced Computer Science and Applications(IJACSA), 5(9), 2014.

Intensity Weighted Histogram Equalization Method for Night Vision

Ernesto Zamora Ramos

Computer Science Department, University of Nevada, Las Vegas, United States;
zamorara@unlv.nevada.edu

ABSTRACT

This paper explores the possibility of utilizing histogram equalization on images captured in poor lighting conditions in order to expand their histogram dynamic range, enhancing their contrast and effectively provide night vision for such images. Then, some drawbacks of standard histogram equalization for dark images, caused mainly due to the clustering of pixels around the lowest intensities are exposed, and Enhanced Intensity Weighted Histogram Equalization is presented as a solution to obtain more realistic night vision images by incorporating the normalized weight of each pixel intensity into the calculations and spreading the histogram values to fill in the gaps, reducing noisy high frequency changes. This technology can be applied to new capture devices that detect the lack of illumination and engage Enhanced Intensity Weighted Histogram Equalization to provide low light capture, useful for surveillance, driving, medical imaging, and even space exploration.

Keywords: night vision, histogram equalization, contrast enhancement, image enhancement.

1   Introduction

It is well known that histogram equalization (HE) is a method utilized in digital image processing to enhance the contrast of an image. It works by expanding the dynamic range of the image histogram.

In the histogram for an image with poor contrast, it can be seen that all pixels are clustered close together around a few intensities. After applying histogram equalization to the image, it is observed how the pixels are no longer clumped together, but their intensities have been spread, trying to expand over the whole range of the histogram. This increased distance between intensities translates in an increased contrast for the image as it can be seen in figure 1.

Note that for this discussion, it is assumed, unless otherwise specified, that digital images have been converted to grayscale using the intensity value of each pixel, also known as luma or Y component in the YUV color space, computed from the RGB color space as standardized by International Telecommunications Union in BT.601-7 [5].
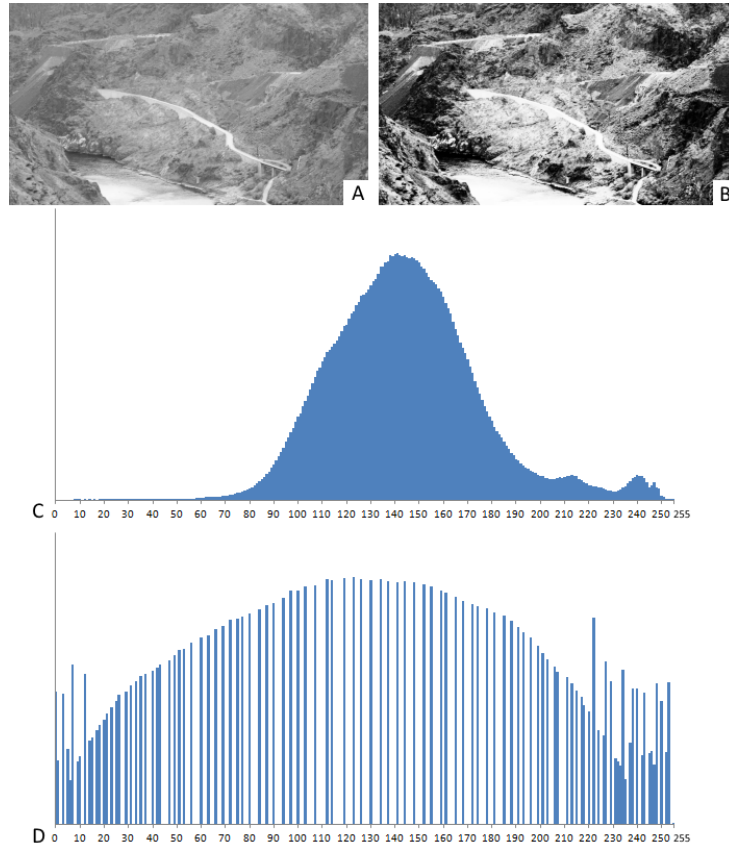
Figure 1. Poor contrast image before and after equalization. A) original image; B) image after histogram equalization; C) histogram of image A (notice how most pixels are clustered around a peak intensity);. D) histogram of image B (notice how the intensities have been spread apart).

HE accomplishes its goal by applying a non-linear transformation to the image in question. It computes the cumulative distribution function (CDF) of the histogram of the image, and then uses it as a look up table for the new pixel intensity values in the resulting image. Table I shows the definition of the classic HE algorithm.

Now, notice that the histogram for images captured with commercial digital cameras under poor illumination conditions is similar to that of an image with low contrast, but the intensities are closer to zero (see figure 2).

Table 1: Classic Histogram Equalization Algorithm [8]

Let I be the original image.

Let I(i) be the intensity of pixel i in the image. $0 \leq I(i) \leq X_h$. X_h is the upper bound of the intensity. Typically $X_h = 255$.

Let N be the number of pixels in I.

Let H be the histogram of I. This is, H(x) is the number of pixels in I such that I(i) = x.

Let $f(x)$ = H(x) / N, be the probability function for a pixel in I to have intensity x.

Let $F(x) = \sum_{n=0}^{x} f(n)$, be the CDF for $f(x)$.

Then, the resulting image is defined as $I'(i) = X_h \cdot F(I(i))$.

If HE is applied to poorly illuminated images, the result is a clearer picture. The little energy captured is amplified, lighting up the original image, and making the shapes visible to the human eye (see figure 3).

It is clear that if image capture devices are equipped with means of detecting low illumination and small dynamic ranges in the histogram of the capture, the subsequent captures can be subject to some variant of HE to improve contrast and effectively perform night vision via software. Such devices can be used as an alternative option to current and more expensive night vision devices such as infrared or

Figure 2. Image captured with poor illumination and its corresponding histogram. Notice how the intensities are clustered together, akin to an image with poor contrast.
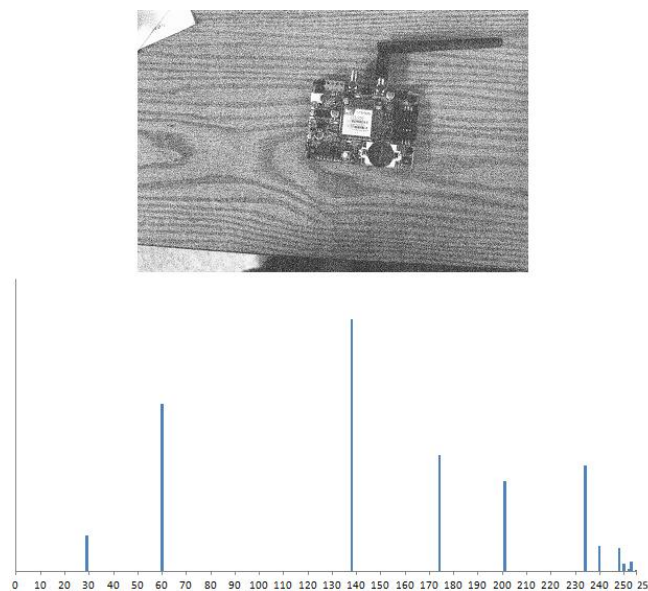
Figure 3. Image captured with poor illumination and its corresponding histogram. Notice how the intensities are clustered together, akin to an image with poor contrast.

thermal cameras and to improve current camera technology, ubiquitous in automobiles [4, 6], cell phones and other wearables. These cameras can also be very useful for surveillance, nocturnal observations such as wildlife and deep ocean exploration, medical imaging enhancement, search and rescue, and even space exploration.

However, after several experiments, it can be noticed that HE fails to expand the histogram to the whole dynamic range in dark images. Observe that an undesired artifact of applying HE as an alternative to enhance poorly illuminated scenes is the washed out, overly bright nature of the result. The reasons for this behavior were determined and a variation of the algorithm was developed that results in sharper images with better contrast where the whole range of the histogram is utilized.

The rest of this paper discusses some of the work done relating to software night vision and HE, followed by the exposition of the proposed modifications to HE and enhancements; concluding with some experimental examples of the improved results.

2 Related Work

Even though standard HE offers a direct alternative for the enhancement of dark images, in many occasions the resulting images are too bright, or washed out, so, there have been several works that propose improvements upon this technique in general, and for the purpose of night vision.

There are many variations to the HE algorithm. Many of these try to increase the contrast and dynamic range of an image while preserving the brightness or expected intensity value with the purpose of applying it to images with low contrast, but not specifically for poorly illuminated images.

In their work "Contrast Enhancement Using Brightness Preserving Bi-Histogram Equalization" [10], the authors explain a popular variation of standard HE, called Bi-Histogram Equalization (Bi-HE). This is one of several variations to HE that pursues to maintain the image average intensity while expanding the dynamic range. Bi-HE seeks to divide the image histogram into two histograms separated by the mean value. standard HE is then performed on each sub-histogram. Methods like this are introduced in an attempt to make HE viable in consumer electronics by lessening the artifact of brightness change in an image after equalizing it.

Chen and Ramli [9] propose a variation of Bi-histogram equalization where they apply Bi-HE recursively. Each new section of histogram delimited by its bounds or means is subjected to Bi-HE once again, and so on.

Another variation divides the image into regular regions of equal area and apply HE to each region so that the variance of the intensity is smaller in the locality and does not affect the result as drastically as the global variance [8]. The result, however, is a patchy image with unnaturally bright areas.

While histogram equalization methods that preserve brightness could be useful to enhance images with poor contrast, they may not be as appropriate to utilize for poorly illuminated images because the intention is to increase their contrast as well as to brighten them up. These methods also tend to suffer from the same downside as standard HE when applied to dark images as explained later in this paper.

However, histogram equalization has only been used in a limited amount of work as a night vision alternative. Many authors have also realized that standard HE and variations used in other types of images need to be modified in order to provide better results for dark images.

In his thesis work [2], Teo realizes that HE, or one of its variants, can be applied to night vision images to enhance their contrast and improve further on the quality of visuals. The author, however, applies the technique to images already captured with night vision or thermal imaging devices, so, the effect of HE on these images is not as pronounced as when applied directly to the original dark images.

In their paper "New image enhancement algorithm for night vision," [11] the authors propose a combination of HE and contrast enhancement to improve upon standard HE when used for dark

images after realizing the unnatural increase in brightness in resulting images when applied for night vision.

Sapkota [7] shows in his work the application of the concept, already explaining the possibility of building a capture device that utilizes HE to provide night vision for low light environments. He goes on to explain Incremental Histogram Equalization to look for the optimal upper bound of dynamic range expansion of the histogram where the resulting image would more closely resemble the well illuminated version. The author, however, still uses the standard HE algorithm from table I to obtain the night vision result, just varying the upper bound X_h to find the peak of signal to noise ratio.

In most of these papers, the variations to the standard HE provide some improvement on the resulting images, however, almost none addressed the issue that HE, in fact, does not expand the histogram to the whole dynamic range for poorly illuminated images as it does for better lit images.

3 Proposed Intensity Weighed Histogram Equalization

Observe how the result from applying HE to a dark image usually looks washed out, and overall, too bright (see figure 3), making some details close to the higher intensities practically indistinguishable. This is one of the undesired artifacts introduced by the equalization process. Studying the histograms of resulting images closely, the cause of this undesired effect can be identified and the technique can be adjusted accordingly.

On dark images, the zero and close to zero intensities are predominant, and their effect is what causes the phenomenon highlighted in the histogram in figure 4. Applying classic HE to most images will cause this effect. Notice from the definition of the algorithm in table 1 that if there are pixels with zero intensity, then $F(0) = u > 0$. So, in the new image all pixels will be $I'(i) \geq u \cdot X_h$. This means that the gap highlighted in figure 4 is of magnitude u intensities. The main problem with this incident is that classic HE will not map successfully the pixels to the dynamic range of the histogram when applied to dark images. Also, no matter what, pixels that would actually have zero intensity, will be given an artificial value.

Intensity Weighted Histogram Equalization (IWHE) is the proposed solution to this problem. It is a variation of the standard HE, and it is also a global equalization method (i.e. it operates over the whole image instead of smaller regions). The main modification in IWHE consists on replacing the computation of the resulting image with the formula:

$$I'(i) = \min\left(X_h \cdot F\big(I(i)\big) \cdot \frac{I(i)}{limitY}, \ X_h \right) \tag{1}$$

Where $0 < limitY \leq X_h$ is the intensity value where a desired percentage of the pixels have already appeared.

Experimental results suggest that the best quality images are obtained when the value for *limitY* satisfies:
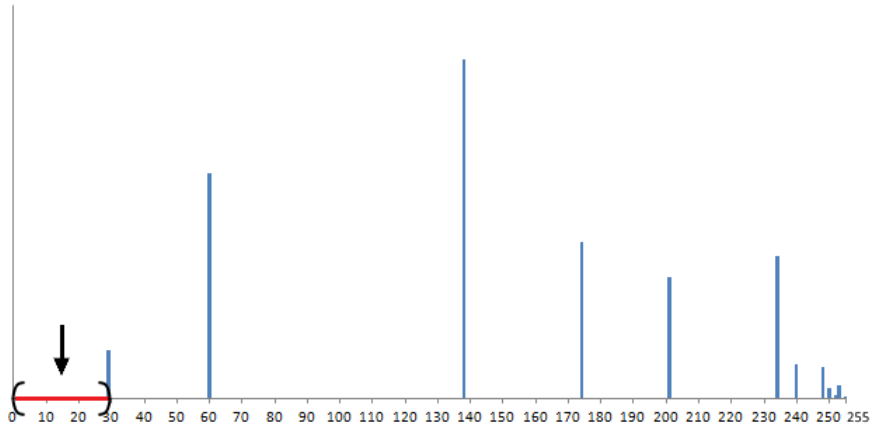
Figure 4. Lapse in intensities before the lowest intensity appears in the histogram for an equalized poorly illuminated image using classic HE.

$$0.97 \le \frac{\sum_{n=0}^{limitY} H(n)}{N} \le 0.99 \qquad (2)$$

That is, *limitY* is the intensity value in the histogram where 97% to 99% of all pixels in the original image have been accounted for. The smallest intensity where 100% of pixels have been counted is ideal to spread all pixel intensities across the whole dynamic range (0, X_h), but the image may still be a little dark because there is usually a small amount of pixels spread among the intensities after 99% of pixels have been counted. The outlying 1% of the pixels should be set to maximum intensity while spreading the rest.

The parameter *limitY*, within reasonable values, can be used, in effect, to control the brightness of the resulting image. It inversely affects the overall brightness. Larger values offer more spread of the intensities, but reducing the brightness. Smaller values can cause loss of information because too
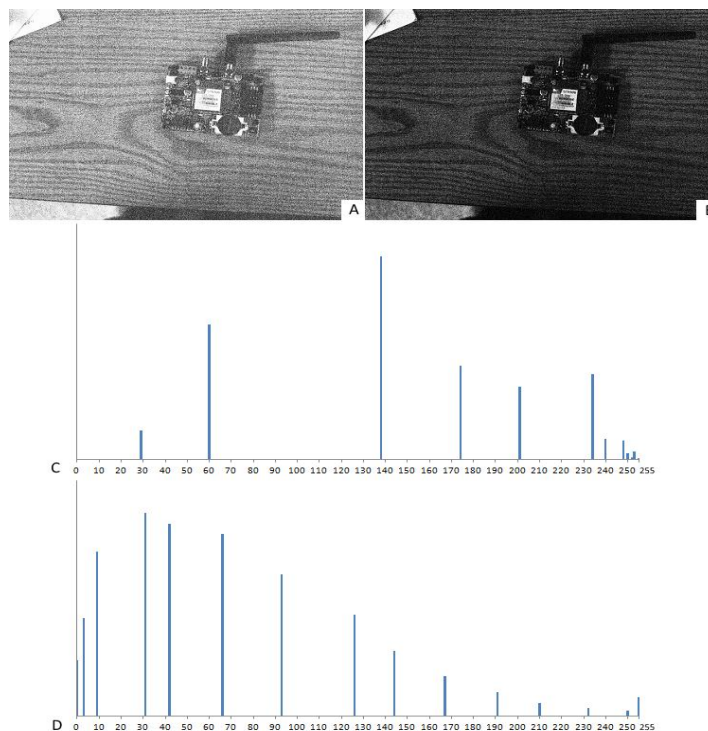
Figure 5. A) classic histogram equalization of image in figure 2; B) Intensity Weighted Histogram Equalization of same image; C) histogram for image A; D) histogram for image B.

many pixels will be moved to full intensity.

The expression $\dfrac{\mathrm{I}(i)}{limitY}$ used in the new formula to compute the resulting intensity considers the normalized weight of the pixel intensity when expanding the dynamic range of the histogram. The result, as seen in figure 5, is an image that looks more natural, no longer washed out, more detailed, and arguably less noisy than its classic histogram equalized counterpart. Even the text and bar codes engraved on the chip are visible and readable. Observe that the resulting histogram has the values spread over the whole range instead of starting with a constant gap, and the pixels are distributed over more intensities. The new equalization also ensures that pixels with originally zero intensity, remain at zero. Black pixels had no energy captured by the camera, and thus it is artificial to give them values too high. This result was achieved after applying IWHE with a *limitY* that satisfies

$$\frac{\sum\limits_{n=0}^{limitY} H(n)}{N} = 0.98 \text{ (refer to equation (2)).}$$

4   Enhanced Intensity Weighed Histogram Equalization

As it can be seen in figure 5, when a poorly illuminated image is enhanced with IWHE, the resulting histogram has expanded to take over the whole dynamic range and it retains a shape similar to the original image histogram, thus giving the resulting image a more natural look.

Note that the resulting histogram is still a comb containing gaps between intensity values giving the image sharp jumps in intensity among pixel regions. To improve upon this, the pixels can be distributed around their representative intensity value in a normal-distribution-like pattern.

Buckets are created around each individual intensity in the resulting histogram of IWHE. For each bucket, the left limit is defined to be the value halfway between the representative intensity and the neighbor intensity to the left. The right limit is defined in a similar manner. Afterwards, the limits of each bucket are extended based on its size to overlap with adjacent buckets (i.e., larger buckets receive a larger extension to each side). See figure 6.
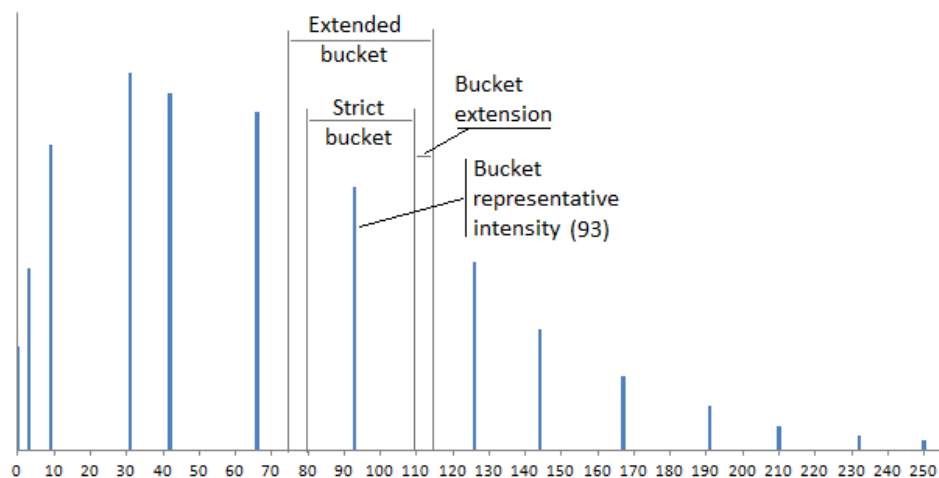
Figure 6. Depiction of a bucket around a representative intensity (in this case, intensity value 93). Strict bucket limits are the halfway values between intensities. The extended bucket is the final bucket and is computed by adding the bucket extension to each side of the strict bucket to achieve overlap between buckets.
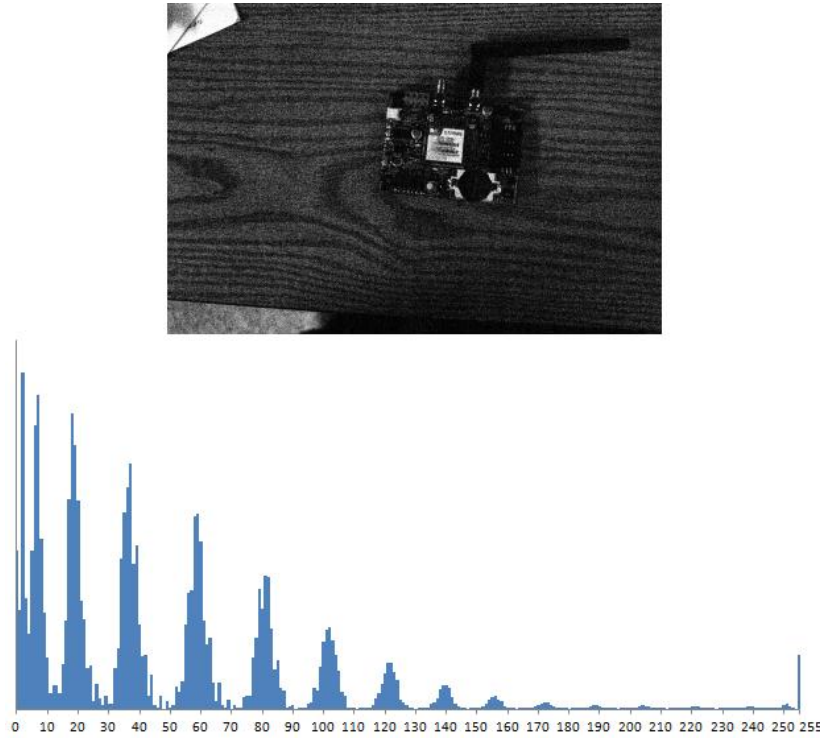
Figure 7. Result of applying Enhanced IWHE to the poorly illuminated image from figure 2. Notice how the histogram distribution has values over the whole range without holes.

The N_8 vicinity of a pixel p is the collection of pixels (including p) in the 3x3 matrix of pixels centered at p. The IWHE result is passed through a filtering mechanism where a new intensity value $I_1(p)$ is computed based on the intensity of the pixels in the N_8 vicinity of p (for the experiments, the average of the intensities was used, but any other filter that can spread the values in the bucket as defined works as well).

$$I_1(p) = f\left(I\left(N_8(p)\right)\right) \tag{3}$$

Then, the range $\Re$ delimited by $min(I(p_i))$ and $max(I(p_i))$ is mapped linearly to the range $\Re'$ for the bucket corresponding to the intensity of p. The intensity value for p in the final image, $I'(p)$, is the value $I_1(p)$ mapped from $\Re$ to $\Re'$:

$$I'\left(I_1(p)\right): \Re \to \Re' \tag{4}$$

Figure 7 shows the final result and histogram obtained after applying this method to the dark image in figure 2. The images enhanced with this method present reduced noise on areas where uniform intensity is expected due to the attenuation of high frequency regions.

5   Experimental Results

A collection of pictures was captured with two different commercially available cameras with no night vision capabilities (other than flash) under poor light conditions. The variety of images included night time landscapes as well as objects captured in a closed room without illumination.

Figure 8. Visual comparison between standard HE and Enhanced IWHE. Images are arranged in pairs where the left image of the pair was obtained through the application of standard HE to a poorly illuminated scene and the right image was obtained through the application of Enhanced IWHE to the same image. Top-left: book; top-right: the moon (original photo obtained from NASA website); center-left: marker; center-right: circuit board; bottom-left: apartment complex parking lot at midnight; bottom right: computer keyboard.

Figure 8 shows a visual comparison between the application of HE and Enhanced IWHE to improve some of the poorly illuminated images captured. The original images are omitted because their poor illumination offers no meaningful detail. With both cameras, the obtained pictures were nothing more than dark images much like figure 2. Notice how images treated with Enhanced IWHE retain a more realistic look and details than their washed out, surreal HE counterparts.

Available upon request are the C# program used for the experiments, a Windows Store App demonstrating proof of concept, and the original version of all images utilized for this study.

6 Conclusions

Histogram equalization is an inexpensive method to increase the contrast in an image that can be utilized to enhance visibility in poorly illuminated scenes, effectively providing night vision capabilities. Although, dark images receive improved lighting when equalized, the results look washed out and unnatural, due to the concentration of pixels with zero intensities, and their histogram shows a comb-like shape with large gaps between intensities. The introduction and application of Enhanced Intensity Weighted Histogram Equalization as a global equalization technique tackles these problems by considering the normalized weight of each pixel when equalizing the image, expanding the histogram to utilize the whole dynamic range, producing crispier, more natural looking, more detailed and less noisy results than standard histogram equalization for dark images.

This technology can be embedded in capture devices that engage Enhanced IWHE when a small dynamic range is detected on the input image histogram, with values clustered close to lower intensities, as a less expensive alternative to other night vision technologies, such as infrared cameras. This will provide enhanced images from captures in low light environments, useful in cameras employed for surveillance, driving, search and rescue, observation of wild life at night or deep ocean, medical imaging enhancement, and many others.

REFERENCES

[1]   A. Waxman, D. Fay, P. Ilardi, D. Savoye, R. Biehl, D. Grau, "Sensor Fused Night Vision: Assessing Image Quality in the Lab and in the Field," *9th International Conference on Information Fusion*, 2006, pp. 1-8.

[2]   C. K. Teo, "Digital Enhancement of Night Vision and Thermal Images," Thesis, *Naval Postgraduate School.* Monterey, California, USA. 2003.

[3]   D. Fay, P. Ilardi, N. Sheldon, D. Grau, R. Biehl, A. Waxman, "Real-time image fusion and target learning & detection on a laptop attached processor," *International Conference on Information Fusion*, 2005, pp. 499-506.

[4]   F. Schule, R. Schweiger, K. Dietmayer, "Augmenting Night Vision Video Images with Longer Distance Road Course Information," *Intelligent Vehicles Symposium (IV)*, 2013 IEEE, pp. 1233-1238.

[5]   International Telecommunications Union. (2015). *BT.601: Studio encoding parameters of digital television for standard 4:3 and wide screen 16:9 aspect ratios* [Online]. Available: http://www.itu.int/rec/R-REC-BT.601-7-201103-I/en

[6]   M. Serfling, O. Loehlein, R. Schweiger, K. Dietmayer, "Camera and Imaging Radar Feature Level Sensorfusion for Night Vision Pedestrian Recognition," *Intelligent Vehicles Symposium*, 2009 IEEE, pp. 597-603.

[7]   N. Sapkota, "Real Time Digital Night Vision Using Nonlinear Contrast Enhancement," MS Thesis. *UNLV Theses/Dissertations/Professional Papers/Capstones*. 2013.

[8]   R. C. Gonzalez and R. E. Woods, "Histogram Equalization," in *Digital Image Processing*, 3rd ed., UP, India: Prentice Hall, 2007, pp. 122–128.

[9]   S. D. Chen and R. Ramli, "Contrast Enhancement using Recursive Mean-Separate Histogram Equalization for Scalable Brightness Preservation," *IEEE Trans. Consumer Electronics*. vol. 49, no. 4, pp. 1301-1309, 2003.

[10]   Y.T. Kim, "Contrast Enhancement Using Brightness Preserving Bi-Histogram Equalization," *IEEE Trans. Consumer Electronics*, vol. 43, no. 1, pp. 1-8, Feb. 1997.

[11]   Z. Yu, W. Xiqin, and P. Yingning, "New image enhancement algorithm for night vision," ICIP 99. Proceedings. *1999 International Conference on Image Processing*, vol. 1, pp. 201-203, 1999.

Drusen Quantification for Early Identification of Age Related Macular Degeneration

[1]Kajal Kumari and [2]Deepti Mittal

[1,2]Electrical and Instrumentation Engineering Department, Thapar University, Patiala (Punjab), India;
kajalkumari0503@gmail.com; deepti.mittal@thapar.edu

ABSTRACT

Age-related macular degeneration (AMD) is a degenerative disorder in people of age 50 and above, in developed nations, characterized on grading of color fundus images by the presence of pathologies such as drusen in macular area. Currently, there is no treatment which can cure irreversible blindness due to age-related macular degeneration. Therefore, the only feasible option is to prevent the incidence of age-related macular degeneration and avoid this unnecessary vision loss. This paper presents an automated method for early diagnosis of AMD by quantifying drusen on the basis of its size, number and area in macular region from standard color retinal images. Previously used methods, generating unsatisfactory results in some cases, are time consuming, complex and prone to error. Therefore, this paper provides a simple drusen detection and quantification method to detect the exact number of drusen , area and size as well as classify drusen into small, intermediate and soft or large which will further help in initial screening of early stage of age-related macular degeneration and its progression i.e. change in drusen area. The proposed method achieved 93.2% accuracy for drusen detection and 91.8% accuracy in small drusen, 98.66% in intermediate drusen and 92.91% in soft drusen quantification in order to grade the severity of AMD which outwits the other methods.

Keywords: Age-related macular degeneration, pixel-wise feature extraction, drusen subtypes, quantification, fundus images.

1   Introduction

Age-related macular degeneration (AMD) is a degenerative disorder of the central area of the retina called macula often associated with visual impairment which is more frequent after 65 years of age in the western world [1-3]. Currently, approximately 35% of adults older than 80 years in the United States are affected by vision loss which is expected to increase approximately 1.5 fold over the next ten years [5]. AMD can be broadly divided into dry and wet [3, 4]. Dry AMD is caused by the lack of functioning of visual cells and generally associated with lesion named drusen and pigmentary changes in the retina [6, 7]. It is also called as early and intermediate AMD and generally associated with only minimal visual symptoms. Late AMD has two types, first one is progressive geography atrophy in the macular region called as late "dry AMD" and second one is an exudative AMD due to development of choroidal neovascularization called as "wet AMD". Wet AMD progresses rapidly and may respond to laser treatment in early stages [6, 8-9]. Most people with macular degeneration are affected by the dry type and there is no treatment for it [10]. Age-Related Eye disease Study (AREDS) showed that the specific anti-oxidant vitamin supplementation reduces the risk of progression from intermediate stage to late AMD stage that can allow for preventive strategies. Currently, there is no cure for AMD, however early detection and subsequent treatment may prevent the severe vision loss or slow the

progression of the disease [11]. Further strategies are developed to control the risk of progression of AMD from intermediate stage to late. To control the risk of progression it will be important to identify the group of people with early signs so that they should be treated at time by providing treatment trials and user interventions. Therefore, identifying people with early signs of the disease and then determining their risk based upon fundus characteristics is more important from social and economic point of view.

Drusen represent the hallmark of non-exudative or dry AMD and considered as one of the first clinical sign of AMD. These are pale yellow deposits of cholesterol and other materials beneath the Retinal pigment epithelium (RPE), identified by the manual evaluation of retinal fundus images by trained clinicians. Many people over the age of 60 will have some drusen which can be classified as hard or soft depending upon their size [12-13]. Hard drusen are small lesions with sharp borders and soft drusen are those with indistinct borders. Soft drusen has been recognized as precursors to advanced AMD. The international Classification and Grading System for Age Related Maculopathy defines hard drusen as having diameters up to 63 microns, intermediate drusen between 63-125 microns and soft drusen which are greater than 125 microns [14]. Existing AMD grading systems require human grader's subjective manual interaction, which is time consuming, prone to inaccuracy, poor repeatability if experienced graders are not used and difficult to maintain intra or inter-rater agreement. Although a number of automated methods have been developed to classify and quantify drusen after detection as explained below with some limitations.

Brandon and Hoover [15] developed a multi-level method to detect drusen by applying wavelet-based feature extraction and Feed Forward Neural Network (FFNN) classifier. It classifies images as normal, large few drusen, large many drusen, fine few drusen, fine many drusen and abnormal drusen. This method did not consider any soft and hard drusen, and distinct and indistinct drusen classification which is an essential step for early detection and grading of AMD. Barriga et al. [16] proposed a method for lesion phenotyping on AMD which will further helped in developing an automated AMD grading system. Amplitude modulation-Frequency modulation (AM-FM) is used to generate multi-scale features for classifying pathological structures such as vessels, retinal background, hard and soft drusen. It was unable to classify distinct and indistinct drusen which is one of the important criteria for AMD grading. Agurto et al. [17] described and evaluated the performance of AM-FM algorithm which was earlier used by Barriga et al. [16]. This algorithm was used to report on the presence and absence of AMD and also successful in detecting the area of drusen but unable to count the number of drusen present in an image. Prasath and Ramaya [18] proposed an automated method for drusen detection and grading of AMD based on GLCM based textural features extraction. This method classified drusen into small, medium and large but some of the samples are misclassified as small drusen. Soliz et al. [19] developed a quantitative assessment method for maculopathy using colour retinal images. They used Gaussian smoothing and probability based thresholding method to quantify drusen and assess longitudinal changes in retinal images presenting with maculopathy following Wisconsin Age-related Maculopathy Degeneration Grading Scheme. A series of manual control tools are provided for a grader to further improve the segmentation results. However, the agreement between the graders on different drusen sizes was only 67%. Smith et al. [20] developed a quantitative assessment method for detecting drusen and its size but unable to grade the severity of AMD. Kumari and Mittal [21] proposed a method for automatic drusen detection and quantification using retinal fundus images. This method was able to calculate the area and number of drusen but did not calculate the size of drusen. Hijazi et al. [22] developed a method which is based on spatial histogram and Case base reasoning approach for classifying image into AMD and non-AMD on the basis of drusen only. It did not calculate size and

area of drusen which was a major step for grading the severity of AMD. Mora et al. [23] proposed a method for automatic drusen detection and quantification using retinal images. This method was able to calculate the size and area of segmented drusen but validated only on twenty-two retinal images. Bhuiyan et al. [24] proposed a method for drusen area quantification and also classified drusen into intermediate and soft but unable to quantify drusen on the basis of area.

In summary, the limitations of previous works on drusen detection for AMD grading are the classification of drusen according to its size and insufficient information regarding quantification of drusen. Therefore in the present work, a method for AMD grading is proposed by (i) finding boundary of drusen using thresholding based segmentation, (ii) classifying drusen into small, intermediate and large or soft and (iii) quantify drusen on the basis of size, area and number. The method, designed in this way, showing comparatively higher accuracy than the other methods, accurate quantification of drusen with 91.8% accuracy for small drusen, 98.66% for intermediate drusen and 92.91% for soft drusen quantification, further contributed to diagnose the AMD.

Table 1. Summary of previous research work related to grading of AMD using retinal fundus images.

Method	Year	Specialty	Image processing techniques	Level of Quantization	Accuracy (%)
Brandon and Hoover [15]	2003	Texture based	Mexican hat wavelet and Feed Forward Neural Network	Drusen or non-drusen Small or large drusen	87 71
Barriga et al. [16]	2009	Texture based	Multiscale feature through Amplitude modulation-Frequency modulation and ROI by partial Least square.	Drusen and non-drusen Soft and hard drusen	Up to 100 96
Agurto et al. [17]	2011	Texture based	Same as Barriga et al.	Drusen area	73
Prasath and Ramaya [18]	2015	Texture based	Morphological operators, circular hough transform, texture descriptors	Classified drusen into small, medium and large	98.5
Soliz et al. [19]	2002	Thresholding based	Median filtering, Gaussian smoothing and probability based thresholding	Drusen and non drusen Drusen size	71 67
Smith et al. [20]	2003	Thresholding based	Otsu and intensity based thresholding	Classified drusen into small, intermediate and large	67
Kumari and Mittal [21]	2015	Thresholding based	Illumination correction, Otsu's thresholding, morphological operation, pixel-wise feature extraction	Drusen area detection	96
Hanafi et al. [22]	2010	Cluster based	Spatial histogram and similarity based classification	AMD and non AMD classification	77
Mora et al. [23]	2011	Edge and template based	Illumination correction, normalization and Gaussian derivative	Drusen area detection Drusen pixel detection sensitivity and specificity	43 68 96
Bhuiyan et al. [24]	2013	Based on region growing	Gaussian derivative and region growing technique	Quantified drusen area Classified drusen into intermediate and soft	82.14

2   Material and method

Materials

Database is a tool for evaluation and comparisons of different algorithms. In order to evaluate algorithms for automated screening and diagnosis of retinal disease, some of the benchmark databases are publicly available. The purpose of these databases is to check the validity of systems and to compare the results with the existing techniques. In this paper, two databases named STARE (Structured Analysis of Retina) and ARIA (Automated Retinal Image Analysis) are used for grading the severity of AMD and to compare the results with the existing methods.

The STARE database is acquired using TOPCON fundus camera with 35 degree field of view and a resolution of 700x605 pixels. It consists of total 400 images form which 36 is for normal AMD and 48 for AMD images [25]. The ARIA database is acquired using Carl Zeiss Meditec fundus camera with 50 degree field of view and a resolution of 768x576 pixels. It consists of 101 normal and 11 AMD images [26] as described in Table 2.

Table 2 Description of database used in the present work.

Database	Camera	Field of view	Resolution	No. of Images	Normal Images	Images with AMD
STARE	TOPCON	35 degree	700x605	400	36	25
ARIA	Carl Zeiss Meditec	50 degree	768x576	450	101	11

Method

The proposed method to grade the severity of AMD consists of three phases named as (i) boundary extraction of drusen (ii) quantification of drusen (iii) grading of AMD severity which is discussed below.
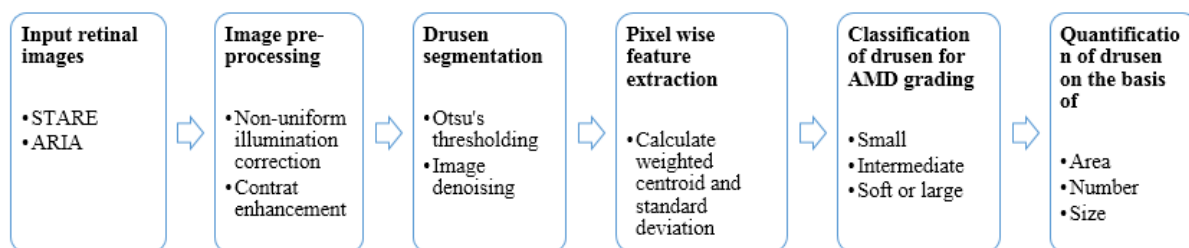
Figure 1. Flow chart of proposed drusen quantification method.

2.1   Boundary extraction of drusen

To extract the boundary of drusen following steps are carried out: firstly the retinal fundus images are preprocessed by selecting green channel for better contrast, non-uniform illumination is corrected by subtracting an approximated image from original image then resultant image is enhanced by using automatic contrast enhancement technique. Drusen is segmented using Otsu's thresholding and unwanted noise is removed by morphological operation. Edge of drusen is detected by using canny edge detector [21].

2.2 Drusen detection

After detecting the edge of drusen, the size, shape and area of each region is analyzed which will further help in grading the severity of AMD. A label matrix is used by Kumari and Mittal [21] to visualize the drusen as a pseudo color indexed image to highlight the drusen area. Position of each drusen is located by using weighted centroid of each region and to highlight the exact number of drusen pixel-wise feature is extracted so that if any drusen is overlapped over other then it can be separate out. Hence the present method provides a platform to diagnose the AMD by locating its position, total number of drusen present in an image as well as by calculating its size and area which is further discussed.

2.2.1 Drusen shape analysis

A drusen is circular or oval shaped region. These shapes are 2-D and for verification whether it is circular or oval, boundary detection plays an important role. In this paper shape is analyzed as circular or oval by visualizing the boundary of drusen. The centroid and boundary point of detected drusen is calculated which will help in computing the ratio of minimum and maximum radius to determine the shape as circular or oval.

2.2.2 Drusen size analysis

After shape analysis, drusen are filtered on the basis of size. Since all drusen are of circular or oval shaped, the diameter of the region in pixels provides the size of the drusen.

2.2.3 Quantification of drusen area

The true area is calculated based on the drusen boundary and region information from the image which includes drusen. To compute the area of drusen, total numbers of pixels are counted as given in Eqn. (1).

$$\text{Area,} \qquad A_i = \sum_{r=0}^{H-1} \sum_{c=0}^{W-1} I_i(r, c) \qquad (1)$$

The area A_i is measured in pixels and it indicates the relative size of the object.

2.2.4 Number of drusen

To count the exact number of drusen present in an image pixel wise feature is extracted by calculating the weighted centroid and standard deviation of each object i.e. drusen using pixel value of grey scale image. It is also useful in locating the exact position of each spot that has been blurred over an image region during image acquisition process. This will also help in decomposition of overlapped objects into individual particle []. Hence one can easily count the exact number of drusen present in a given image.

2.3 Grading of AMD severity

Retinal color fundus imaging has been widely used for AMD grading. A number of grading protocols has been established for drusen grading which helps in identifying the stage of AMD using color fundus imaging. Among these protocols Wisconsin Age-related Maculopathy Grading system, the International Classification and Grading System for Age-related Maculopathy and Age-related Macular Degeneration and its modified version are widely used [27, 14, 28]. These methods mainly use computer software tools that a grader uses to manually count the drusen through drawing different sizes of circles in the software interface. The quantification of drusen and grading of AMD using manual methods over fundus photographs is not commonly used as it is a fastidious process and lacks reproducibility. Also, the variability within the analyses performed by different

ophthalmologists limits the use of this technique. Hence, automated AMD grading techniques are used for the diagnosis of disease severity level. There are a number of articles have been published on drusen quantification using retinal fundus imaging but out of these only a few of them are utilized drusen size, area and actual number in the image to grade the AMD severity as explained in the literature review section as well as only a few of techniques can classify into small, intermediate and soft. Most of these automatic techniques are constrained in determining the drusen segmentation level and absence and presence of drusen in the retina.

In this paper, an automatic, accurate and efficient classification and quantification of drusen with considering drusen position, size, shape, area and actual number of drusen present in retinal fundus images can provide a useful tool to define the severity of AMD. Use of such tool would help to determine the severity of risk for progressive sight threatening advanced AMD. AREDS grading system defines the AMD category as 1 to 4 - normal to severe AMD based on the drusen, geography atrophy, retinal pigment epithelium and neovascularization following Wisconsin grading protocol which is applied in this paper. The study defines AMD category as 1 if there is no drusen exists or drusen size < 63 μm and total area covered by drusen is < 125 μm. AMD category 2 or intermediate is defined as drusen size $\geq$ 63 μm and < 125 μm and drusen area $\geq$ 125 μm but GA absent. AMD category 3a is defined as intermediate $\geq$ 63 μm and < 125 μm, drusen area 360 μm diameter circle if soft distinct drusen are present and $\geq$ 656 μm diameter circle if soft indistinct drusen are present as illustrated in Table 3 [29].

AMD Category	First Eye			Second Eye
	Drusen size	Drusen Area	Pigment Abnormalities	
1	None or small (< 63 μm)	< 125 μm diameter circle (5-15 small drusen)	None	Same as first
2	Small (< 63 μm) or intermediate ($\geq$ 63, >125 μm) Doesn't matter if pigment abnormalities present.	$\geq$ 125 μm diameter circle. At least one drusen.	Absent or present, but GA absent.	Same as first or category 1.
3a	Intermediate ($\geq$, <125 μm) or Large ($\geq$125 μm). None required if non central GA present.	$\geq$ 360 μm diameter circle if soft indistinct drusen are present (=20 intermediate drusen). $\geq$ 656μm diameter circle if soft indistinct drusen are absent. At least one drusen should present.	Absent or present but GA absent.	Same as first or category 1 or 2.
3b	First eye same category as 3a.			Visual Acuity <20.32 due to AMD; or unicolor disqualifying disorder present.
4a	First eye same category as 1, 2 or 3a.			Advanced AMD.
4b	First eye same category as 1, 2 or 3a.			Visual Acuity <20/32 due to AMD, but advanced AMD not present.

3   Evaluation method

In this paper, detected drusen with quantification by proposed method is compared with manually graded retinal images. Thirty four images from STARE and ARIA datasets are randomly selected with variety of drusen types. The performance is measured in different steps:

3.1   Drusen detection accuracy

It presents the percentage of retinal images with the presence or absence of drusen detected correctly. Segmented drusen from proposed method are compared with ground truth in terms of sensitivity, specificity, accuracy, positive predictive value (PPV) [30-31]. These performance parameters are computed considering drusen pixels positive and background pixels negative which are discussed below. Here T_P are true positive means drusen regions correctly classified or number of overlapped positive pixels in drusen and ground truith images. T_N, are true negative means non drusen regions correctly classified. F_P, ar false positives means non drusen regions wrongly classified as drusen regions. F_N, are false negatives means drusen regions wrongly classified as non drusen regions.

$$\text{Sensitivity} = \frac{T_P}{(T_P + T_N)} \tag{2}$$

$$\text{Specificity} = \frac{T_N}{(T_N + F_P)} \tag{3}$$

$$\text{Accuracy} = \frac{(T_N + T_P)}{(T_N + T_P + F_N + F_P)} \tag{4}$$

$$\text{PPV} = \frac{T_P}{(T_P + F_P)} \tag{5}$$

3.2   Non-overlapped drusen area

To measure the non-overlapped area, comparison of segmented drusen by proposed method and same with ground truth is done. Here comparison is done pixel-by-pixel to find the true size and area of drusen.

3.3   Numbers of drusen

To measure the accuracy of drusen types thirty four images are selected which includes small, intermediate and soft or large drusen. Afterwards, numbers of each drusen type in the individual images are counted for both manually measured and automatically detected. Here accuracy is computed in percentage for different drusen types and also compared with other existing methods.

4   Results and discussion

The proposed method for classification and quantification of drusen is implemented in MATLAB version 7.10 on a PC with Intel core i3 (2.40GHZ) processor. This method is applied on 36 images, publically available datasets i.e. STARE and ARIA, acquired by the fundus camera to diagnose the severity of disease. In this study, automated detected drusen by Kumari, Mittal [21] is compared with manually graded retinal fundus images i.e. ground truth. The performance is evaluated by measuring the drusen detection sensitivity, specificity, accuracy and positive predictive value (PPV) of 82%, 91.3%, 93.2% and 92.21% respectively as absent or present of drusen in the image.

4.1   Boundary detection of drusen

To detect the boundary of drusen, green channel is selected from an image for better contrast and non-uniform illumination is corrected by subtracting approximated image from an original image.

Afterwards, image with uniform illumination is carried out to obtain more information in terms of better contrast with less noise by using automated contrast enhancement technique and morphological operation respectively [32-33]. Further, drusen is segmented by using Otsu's thresholding and boundary is detected by using conventional canny edge detector as described in method of Kumari and Mittal [21]. Fig. 2 represents the boundary of detected drusen by Kumari and Mittal [21].
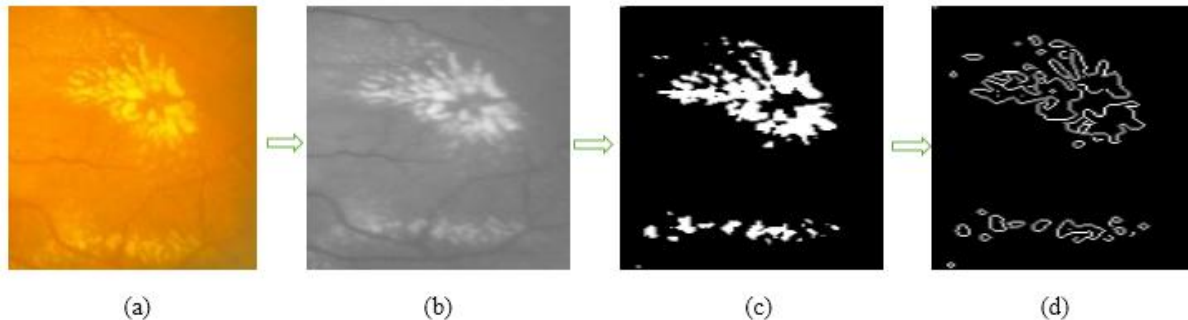
Figure 2. Result of boundary detectioon of drusen: (a) original image (b) green channel of image, (c) segmented drusen, (d) boundary of detected drusen.

4.2   Classification and quantification of drusen

In this paper drusen are classified as small, medium and large on the basis of AREDS categories and quantification is done according to drusen area, size and number present in an image as given in Table 4. Here area is obtained by computing the overall drusen area covered in the macular region by summing the individual drusen area and size is measured in terms of drusen diameter. These values are then converted into micrometers in order to be comparable between images with different resolutions. Here 1 pixel=7microns is used to convert the pixels into microns.

4.3   Performance measure

After quantification of segmented drusen it is compared with the ground truth i.e. manually segmented drusen as shown in table 4. Proposed method has achieved 93.2% drusen detection accuracy, 82% sensitivity, 91.3% specificity and 92.21% PPV. After comparing results of proposed method with ground truth it can be concluded that the present system having better results with less non-overlapped drusen region ranging from 0 to 3.156 for small drusen, 0 to 14.329 for intermediate drusen and 0.72 to 19.41 for large or soft druse. It can be clearly seen from the table 5, the proposed method achives average accuracy of 91.8% for small drusen, 98.66% for intermediate drusen and 92.91% for large or soft drusen, outwits the results of Bhuiyan et al. [24]. The results demonstrated that the proposed system could identify all the intermediate drusen and took less time of 0.042 seconds to quantify the drusen area.

5   Conclusion

Previously, several methods are implemented to segment, classify and quantify the drusen area to measure the severity of AMD in retinal fundus images. This direct method are limited due to user involvement for ROI selection, varying image conditions and lack of adaptive capabilities of the methods, results in poor segmentation and quantification such as over or under segmentations in some parts of the image as well as it requires large computational effort. Therefore, an early treatment and effective planning by using computerized method is highly reliable and may reduce the progression of disease and also provide timely treatment after quantifying drusen which helps in grading the severity of AMD. In this work, an automated segmentation approach has been developed

to classify and quantify drusen for grading the severity of AMD using publicly available retinal fundus images. It analyzes region properties of image by extracting the feature from the pixels of fundus images which will help in decomposition of overlapped objects to evaluate the exact number of drusen. This method will help in computing the total area affected by drusen in pixels with its size, shape and number present in an image. The proposed method outperforms the other existing method by achieving 82% , 91.3%, 93.2% and 92.21% for sensitivity, specificity, accuracy and PPV respectively in addition with accuracy of 991.8% a for small drusen, 98.66% for intermediate drusen and 92.91% for large or soft drusen with less non-overlapping area as compared to ground truth. It can be concluded that the use of the proposed detector may reduce the irreversible blindness across the world and give reliable results in treatment of disease.

Table 4. Classification and Quantitative analysis of drusen to grade the severity of AMD.

	Images	Total no. Of drusen by the ground truth	Total drusen area in the ground truth (μm^2)	Size of drusen (μm)	Total no. Of drusen by the proposed method	Total drusen area by the proposed method μm^2	Size of drusen in μm	Non-overlapped area
SMALL	IM0013	4	73.58	46.508	4	72.85	46.508	0.00
	IM0015	12	1.362×10^{11}	39.627	10	1.0035×10^{11}	36.471	3.156
	IM0046	15	63.84685866	98.899	12	73.84675856	98.880	0.019
	IM0262	9	2.028×10^{10}	52.829	8	1.997×10^{10}	51.064	1.765
	IM0401	6	1.317×10^{10}	48.752	6	1.188×10^{10}	48.518	0.234
	IM0402	5	$1.173481523 \times 10^{10}$	25.975	5	$1.021730348 \times 10^{10}$	25.135	0.84
	Images	Total no. Of drusen by the ground truth	Total drusen area in the ground truth (μm^2)	Size of drusen (μm)	Total no. Of drusen by the proposed method	Total drusen area by the proposed method μm^2	Size of drusen in μm	Non-overlapped area
INTERMEDIATE	IM0006	35	1.973×10^{11}	72.002	33	1.581×10^{11}	63.446	8.556
	IM0007	18	1.263×10^{11}	68.271	18	1.240×10^{11}	68.116	0.155
	IM0012	46	1.463×10^{11}	74.002	43	1.365×10^{11}	62.436	11.566
	IM0033	87	2.033×10^{11}	106.111	87	2.025×10^{11}	104.028	2.083
	IM0038	25	1.168×10^{10}	67.002	25	1.002×10^{11}	64.363	2.639
	IM0066	50	2.209×10^{10}	103.981	50	2.368×10^{10}	95.652	14.329
	IM0068	125	1.689×10^{10}	63.932	125	1.653×10^{10}	63.500	0.432
	IM0079	40	1.135×10^{10}	69.842	36	1.026×10^{11}	69.225	0.617
	IM0097	20	1.139×10^{10}	127.854	20	1.133×10^{10}	127.854	0.0
	IM0192	136	2.603×10^{12}	118.295	136	2.031×10^{12}	118.268	0.027
	IM0263	89	1.759×10^{10}	72.654	89	1.708×10^{10}	72.652	0.002
	IM0376	2	90.985	127.541	2	90.977	127.541	0.008

	Images	Total no. Of drusen by the ground truth	Total drusen area in the ground truth (μm^2)	Size of drusen (μm)	Total no. Of drusen by the proposed method	Total drusen area by the proposed method μm^2	Size of drusen in μm	Non-overlapped area
LARGE or SOFT	IM0003	124	3.782×10^{11}	157.241	119	3.255×10^{11}	157.002	0.239
	IM0037	45	2.511×10^{11}	152.115	45	2.156×10^{11}	150.221	1.894
	IM0041	125	1.984×10^{11}	92.475	120	1.664×10^{11}	92.036	0.439
	IM0063	56	3.620×10^{10}	248.708	52	3.160×10^{10}	248.521	0.187
	IM0143	27	9.484×10^{10}	336.125	27	9.454×10^{10}	336.020	0.105
	IM0147	33	3.329×10^{11}	183.6320	33	3.332×10^{11}	183.613	0.019
	IM0148	41	5.113×10^{11}	82.366	41	5.039×10^{11}	82.285	0.081
	IM0265	43	1.201×10^{10}	176.24	40	1.386×10^{10}	174.625	1.615
	IM0266	98	6.935×10^{10}	558.68	94	6.283×10^{10}	539.27	19.41
	IM0267	112	1.496×10^{10}	669.252	106	1.251×10^{11}	652.395	16.857
	IM0270	10	5.174×10^{10}	152.231	10	5.135×10^{10}	152.135	0.096
	IM0271	26	7.132×10^{10}	119.565	26	7.083×10^{10}	119.327	0.238
	IM0281	31	2.219×10^{10}	560.013	31	2.218×10^{10}	556.916	3.097
	IM0288	39	3.998×10^{11}	146.522	36	3.081×10^{11}	143.366	3.156
	IM0382	82	2.676×10^{11}	445.22	82	2.580×10^{11}	444.50	0.72
	ARIA_13	96	5.073×10^{11}	135.236	92	4.998×10^{11}	132.583	2.653

Table 5. Summary of overall accuracy on small, intermediate and soft drusen detection by proposed method and method of Bhuiyan et al. [].

Method	Category	Number of images	Total number of drusen in ground truth	Number of drusen correctly detected	Accuracy (%)
[25] **Proposed method**	Intermediate drusen (63-125 μm)	12	49	39	79.59
	Soft drusen (> 125 μm)		28	23	82.14
	Small drusen (<63 μm)	**6**	**49**	**45**	**91.8**
	Intermediate drusen (63-125 μm)	**12**	**673**	**664**	**98.66**
	Large or soft drusen (> 125 μm)	**16**	**988**	**918**	**92.91**

REFRENCES

[1]. Lim LS, Mitchell P, Seddom JM et al. Age-related macular degeneration.t, 2012. 379: 1728-1738.

[2]. Bartlett and Eperjesi. use of fundus imaging in quantification of age-related macular degeneration. Surv Ophthalmol, 2007. 52: 655-671.

[3].   Wong, Liew et al. clinical update: new treatments for age-related macular degeneration. Lancet, 2007. 370: 204-206.

[4].   Wong and Rogers. Statins and age-related macular degeneration: time for a randomized controlled trial? Am J Ophthalmol, 2007. 144: 117-119.

[5].   Age-related Eye Disease Study Research Group. The age-related eye disease study system for classifying age-related macular degeneration from stereoscopic color fundus photographs: the age-related eye disease study report number 6. 2001;132:668-681.

[6].   De Jong, *Age-related macular degeneration*. The New England Journal of Medicine, 355(14), 2006. p: 1474-1485.

[7].   Kanagasingam, Bhuiyan et al. Progress on retinal image analysis for age related macular degeneration, Progress in Retinal Eye Research, 2014. 38:20–42.

[8].   Lim, Laude et al. Age-related macular degeneration: an Asian perspective. Ann. Acad. Med. Singapore, 2007. 36 (10), S15.

[9].   Mitchell, Smith, Attebo et al. Prevalence of age-related maculopathy in Australia. The Blue Mountains eye study, Ophthalmology, 1995. 102 (10):1450–1460.

[10].   A.-R.E.D.S.R. Group.A randomized, placebo-controlled, clinical trial of highdose supplementation with vitamins c and e, beta carotene, and zinc for agerelated macular degeneration and vision loss: AREDS report no. 8, Arch. Ophthalmology, 2001. 119 (10):1417–1436.

[11].   Wong, Chakravarthy et al. The natural history and prognosis of neovascular age-related macular degeneration: a systematic review of the literature and meta-analysis. Ophthalmology, 2008. 115: 116-126.

[12].   Chopdar, Chakravarthy et al. Age related macular degeneration.British Medical Journal, 2003. 326 (7387):485–488.

[13].   Mookiah, Acharyaet al. Computer-aided diagnosis of diabetic retinopathy: A review. Computer in Biology and Medicine, 2013. 43 (12):2136–2155.

[14].   Bird, Bressler et al. An international classification and grading system for age-related Maculopathy and age-related macular degeneration. The International ARM Epidemiological Study Group. Surv Ophthalmol, 1995. 39: 367-374.

[15].   Brandon and Hoover. Drusen Detection in a Retinal Image Using Multi- Level Analysis. LNCS, 2003. 618-625.

[16].   Barriga, Murray, Agurto, Pattichis et al. Multiscale AM-FM for lesion phenotyping on age-related macular degeneration. INSPEC, 2009. p: 1-5.

[17]. Agurto, Barriga, Murray et al. Automatic detection of diabetic retinopathy and age-related macular degeneration in digital fundus images. Invest Ophthalmol Vis Sci, 2011. 52: 5862-5871.

[18]. Prasath and Ramaya. Detection of macular drusen based on texture descriptors. Research journal of information technology, 2015. 7 (1): 70-79.

[19]. Soliz, Wilson, Nemeth and Nguyen P. Computer-aided methods for quantitative assessment of longitudinal changes in retinal images presenting with maculopathy. SPIE, 2002. 4681:159-170.

[20]. Smith, Nagasaki, Sparrow et al. A method of drusen measurement based on the geometry of fundus reflectance. Biomedical Engineering, 2003. Online 2: 10.

[21]. Kumari and Mittal. Automated Drusen Detection Technique for Age-Related Macular Degeneration. Journal of biomedical engineering in medical imagiong, 2015. 2:18-26.

[22]. Hanafi, Hijazi, Coenen and Zheng. Retinal Image Classification for the Screening of Age-related Macular Degeneration. In: SGAI International Conference on Artificial Intelligence, 2010. p: 325-338.

[23]. Mora, Vieira, Manivannan and Fonseca. Automated drusen detection in retinal images using analytical modelling algorithms. Biomedical Engineering Online, 2011. p: 10: 59.

[24]. Bhuiyan, Kawasaki, Sasaki et al. Drusen detection and quantification for early identification of Age-related macular degeneration using color fundus imaging. Clinical and experimental ophthalmology, 2013. 4: 305. DOI: 10.4172/2155-9570.1000305.

[25]. STARE database. Available at http://www.ces.clemson.edu/~ahoover/stare.

[26]. ARIA database. Available at http://www.eyecharity.com/aria_online.

[27]. Klein, Devis et al. The Wisconsin age-related Maculopathy grading system. Ophthalmology, 1991. 98: 1128-1134.

[28]. Bartlett and Eperjesi. Use of fundus imaging in quantification of age-related macular change. Surv Ophthalmol, 2007. 52: 655-671.

[29]. Age-Related Eye Disease Study Research Group (1999) The Age-Related Eye Disease Study (AREDS): design implications. AREDS report no. 1. Control Clin Trials 20: 573-600.

[30]. Mittal, Kumar et al. Neural Network based focal liver lesion diagnosis using ultrasound images. Computerized Medical Imaging and Graphics, 2011. 35:315-323.

[31].   Chugh, Kaur and Mittal. Exudates segmentation in retinal fundus images for the detection of diabetic retionapthy. International journal of engineering research and technology, 2014. 3: 673-677.

[32].   Mittal, Kumar, Saxenaet al. Enhancement of ultrasound images by modified diffusion method, Medical and Biological Engineering and Computing, 2010. 48(12): 1281-1291.

[33].   Kaur and Mittal. Segmentation and measurement of exudates in fundus images of the retina for detection of retinal diseases. Journal of biomedical engineering and medical imaging, 2015. 2: 27-38.